

CORROSION MECHANISMS IN REFUSE-FIRED STEAM  
GENERATORS RELATED TO SUPERHEATER TUBE FAILURES

by

Zoltan E. Kerekes  
Richard W. Bryers  
Robert E. Sommerland

Research Division  
Foster Wheeler Energy Corporation

INTRODUCTION

The burning of refuse in waterwall-cooled steam generators to reduce its bulk and provide an inexpensive source of energy from a low-sulfur fuel has introduced potential, new corrosion and deposit problems. The cause for alarm that refuse might be a severe fouling and corrosive fuel originated from the European units placed into service in the mid-1960s. Much of the original tube wastage experienced in the European units has been minimized by improvements in design and operation. The progress of various investigation, comprising an extensive literature survey and comprehensive laboratory analyses, are described in this paper. [1] Also included is an investigation of a recent superheater tube that failed after less than 3000 hours of operation. Analysis indicates that the failure was caused not by alkali-chloride attack, but rather by such other minor constituents as lead (Pb) and zinc (Zn).

REFUSE PROPERTIES

Predicting the extent of fouling and corrosion resulting from refuse firing is extremely difficult. Refuse is heterogeneous by nature and undoubtedly varies from time to time, as well as from location to location. Analyses of refuse, particularly its ash-forming constituents, are not frequently made. However, results reported by Wisely et al. [2] and later analyses at the St. Louis demonstration facility provide a comprehensive analysis of prepared refuse. These results become useful when they can be interpreted in terms of past experience with other fuels. The past experience with Illinois coal, North American lignite, Australian brown coals, and East German salty coals indicates that moderate fouling can be expected if the combined alkali content (expressed as  $\text{Na}_2\text{O} + \text{K}_2\text{O}$ ) exceeds a range of 0.4 to 0.7 percent on a dry-fuel basis. [3] Sodium and potassium are not only bad actors as deposit formers, but they are also known to be responsible for severe corrosion problems. This corrosion usually takes place in the furnace and convection passes because of the formation of pyrosulfates and complex alkali iron sulfates.

Chloride and chlorine must be added to the list of potential problem elements by virtue of the polyvinyl chloride (PVC) plastic and salted food residues. Cutler et al. [4] have indicated that the residence time upstream of deposit formations is sufficient for flue gases to approach chemical equilibrium and that oxygen levels are sufficient to ensure that the bulk of the chloride is converted to gaseous hydrogen chloride (HCl) in the flue gas. The presence of chloride in a deposit on the tube surface can play an active role and accelerate the corrosion rate if the environment cycles between oxidizing and reducing conditions. During reducing conditions

the protective oxide layer is destroyed, while the chlorides are building up in the deposit. As conditions become oxidizing the metal surface opens to both reoxidation and chlorination.

#### INITIAL EXPERIENCE IN EUROPE

The initial corrosion and deposit problems were brought out in a series of articles published in the mid-1960s describing severe corrosion problems in furnace and high-temperature gas passes shortly after start-up. [5-12] The corrosion in general occurred on the leading edge of superheater tubes in the first rows of the bundles underneath deposits, where tube-metal surface temperatures exceeded 825°F (441°C) and furnace wall tubes were subjected to reducing conditions. Figure 1 illustrates the areas in which tube wastage was most frequently reported in the Stuttgart unit. The most severe corrosion occurred on radiant superheater walls at tube-metal temperatures of 950°F (510°C) and on waterwalls at tube-metal temperatures of 600°F (316°C). The first furnace-wall tube failures at Stuttgart were reported after 5000 operating hours. [13,14] Hilsheimer [15] reports similar problems at Mannheim after 3000 hours. The problem was corrected by installing studded tubes covered with SiC in the combustion zone. Nowak, [14] Hilsheimer, [15] Maikranz, [16] and Thomen [17] report localized reducing conditions on the front wall of the furnace despite 80-percent excess air supplied to the combustion chamber.

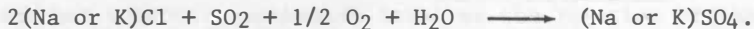
#### CHEMISTRY OF CORROSION

Most investigators have reported that accelerated corrosion often approaches catastrophic proportions when alkali metal chlorides are present with low-melting sulfur-bearing compounds. Explanations of the causes of corrosion in a refuse-fired steam generator can be described by the role of chloride, sulfur, and heavy metal compounds.

##### Role of Chloride

The sources of the chlorine are both inorganic, primarily sodium chloride (NaCl) or potassium chloride (KCl), and organic, primarily PVC plastic. The HCl is released from the PVC during combustion and then combines with Na<sub>2</sub>O or K<sub>2</sub>O to form NaCl or KCl.

The corrosive agent HCl is released by the reaction



The HCl then reacts with the metal surface to form ferrous chloride (FeCl<sub>2</sub>) according to the reaction



It is postulated that metal oxides Fe<sub>2</sub>O<sub>3</sub> or PbO on the tube metal surfaces catalyze the reaction



The chlorine, which is formed only near the catalytic surface, then combines directly with the iron:



The iron chloride can be oxidized according to the reaction

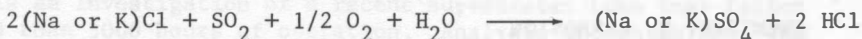


Fassler et al. [18] described the cyclic reaction of chloride corrosion as illustrated in Figure 2.

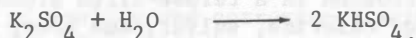
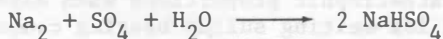
#### Role of Sulfur Compound

The sulfur-bearing compound also plays an important role in low- and high-temperature corrosion in the refuse-fired steam generator. Five sulfur-bearing compounds can form in a refuse-fired steam generator according to the following reactions:

##### Sulfate Formation



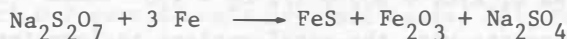
##### Pyrosulfate Formation



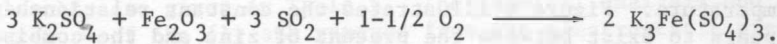
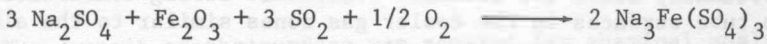
##### Bisulfate Formation



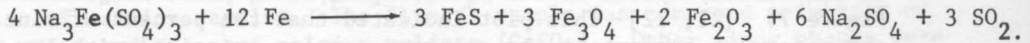
##### Sulfide Formation



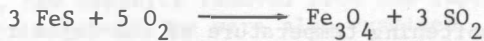
### Complex Sulfate Formation



The molten complex sulfates attack the tube-metal surface according to the reaction



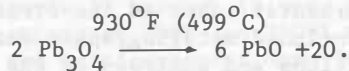
The iron sulfide can be oxidized in the refuse-fired steam generator according to the reaction



The sulfidation and oxidation cyclic reaction described by Cain and Nelson [19, 20] is illustrated in Figure 3. The complete corrosion mechanism of the sulfur compound from firing refuse is shown in Figure 4.

### Role of Heavy Metals

The deleterious effects of lead and zinc salts, particularly chlorides, result from the formation of molten salt layers. The melting points of these salts are low, and when they are mixed with other low-melting chlorides (NaCl, KCl), eutectic compositions form which melt at even lower temperatures. The sources of the Pb and Zn compounds are PVC plastic used as thermal stabilizer or the volatilization of metal scrap in the refuse. Another corrosion mechanism that can occur because of thermal decomposition is



Still another corrosion mechanism involves the reaction of lead chlorides with water at a lower temperature. This reaction results in the liberation of PbO and HCl:



The PbO present in the deposit can accelerate corrosion at a temperature as low as 750°F (399°C). The molten substance acts as a fluxing agent and permeates and destroys the protective oxide layer, resulting in severe corrosion attack. Zinc-like sodium and potassium appear rather consistently in most ashes sampled, running between 5 and 10 percent and generally increasing in concentration with a decrease in gas temperature.

Lead appears somewhat sporadically, ranging from 0 to 11 percent. Presumably these two elements volatilize during combustion and condense on tube surfaces in the cooler gas zones similar to the alkalis. Figure 5 shows the relationship of minor constituents concentration to gas temperature. Figure 6 illustrates the constant relationship that appears to exist between the percent of zinc and the combined percentage of sodium and potassium. If lead is included with the zinc, a linear relationship still exists, but in slightly different proportions. The various deposits collected from refuse deposits composition were plotted in the ternary system of the  $K_2SO_4/Na_2SO_4/ZnSO_4$  phase diagram shown in Figure 7. [21, 22] This plot indicated that the percent of zinc, sodium, and potassium present in the reported samples coincided with low melting temperature phases between 722°F (383°C) and 736°F (391°C), corresponding to 30 to 50 percent  $K_2SO_4$ , 40 to 60 percent  $ZnSO_4$ , and 10 to 30 percent  $Na_2SO_4$ .

The softening temperature of the deposit greatly depends on the total basic constituents present in the bulk deposit. The softening temperature versus ash base content of various deposits from European units and of lignite ash is shown in Figure 8.

Chemical analyses of typical deposit samples collected from various domestic and European refuse-fired units are summarized for comparison in Table 1. The various ash analyses and fusion temperatures of municipal refuse components and slag are tabulated in Table 2.

Defeche [23] also suggests that the tubes act as a catalyst, producing  $SO_3$  from  $SO_2$  in the presence of free oxygen and ultimately forming pyrosulfates and alkaline iron sulfates. His proposed reactions are summarized in Table 3.

#### ANALYSIS OF A RECENT EUROPEAN SUPERHEATER FAILURE

The design and operational data of a recent European refuse-fired steam generator are summarized in Table 4. After about 3000 hours of operation, superheater tubes in the first pass failed. The subsequent investigation included metallographic examination of two of the initial, failed tube sections and analyses of the deposit on the tubes; analyses of fly ash from the electrostatic precipitator; and analyses of deposits from the replacement tubes after 20 days of operation.

The tubes were made of a 1-1/2 in. (38 mm) outside diameter, 0.126 in. (3.2 mm) wall carbon steel material containing 0.30 Mo and designated 15 Mo 3. The ruptured tube samples, covered with a deposit, are shown in Figure 9. Surface appearance of the tube after the deposit was removed by sandblasting and different sections removed for microscopic examination (designated by letter) are shown in Figure 10. The dimensional variation of the wall thickness of tubes at different locations (A through H) are shown in Figure 11. Microscopic examination was conducted to determine if any microstructural change caused by

overheating had occurred during operation. Figure 12 shows the normal microstructure of the tube section.

The deposit on the surface was removed for chemical analysis, and the results are given in Table 5. The chemical analysis and ash-fusion temperature of the fly ash removed from the electrostatic precipitator are summarized in Table 6. X-ray diffraction was used to further determine the various phases present in the fly-ash sample. The two techniques were power camera and diffractometric analysis for the precise identification of the minor phases. Figure 13 shows the X-ray diffraction results. The fly-ash sample was composed primarily of NaCl and KCl, and calcium sulfate ( $\text{CaSO}_4$ ). Other minor phases were identified as sodium aluminum silicate ( $\text{Na}_2\text{Al}_2\text{Si}_5\text{O}_{14} \cdot 5.4 \text{H}_2\text{O}$ ), zinc sulfate ( $\text{ZnSO}_4$ ), and leadoxychloride ( $\text{PbO} \cdot \text{PbCl}_2$ ).

Subsequently, new deposits removed from the replaced superheater tubes after 20 days of operation were also examined. The original superheater tube that failed was replaced by SA-213 T-22, corresponding to 2-1/4 Cr-1 Mo composition. The deposit was characterized by a soft, light color (designated A) at the outer portion of the sample and a hard, dark color (designated B) at the tube/deposit interface. The chemical analyses of these deposits are tabulated in Table 7. The outside, inside, and cross-sectional appearances of the hard B and soft A are shown in Figure 14.

The deposits were mounted in transparent molding material and dry-polished for microscopic analysis. Photomicrographs were taken under polarized light at 100X and 1000X magnification. Figure 15 shows the sintered fly-ash multicomponent deposit of the soft A sample. Figure 16 shows the layer formation in the hard B scale caused by the diffusion of the liquid phase into the metal surface.

A sample of each deposit was analyzed at the inside surface, cross section, and outside surface with a scanning electron microscope (SEM) for microscopic appearance and X-ray analysis using a wavelength dispersive technique. Figures 17 through 19 show the SEM image of the soft A deposit at three locations at 300X and 3000X magnification. Some crystalline habits of the multicomponent deposit associated with glassy cenospheres are clearly visible at high magnification. Particles forming perfect spheroids indicate that the ash must have been molten and solidified at some time in its flight through the combustion chamber. Figures 20 through 22 show the photographs of the wavelength dispersive X-ray chart of the soft A sample at three locations. The major elements Al, S, Cl, Ca, and Zn were detected, but no detectable level of Pb was found in this section of the sample. Figures 23 through 25 show the SEM image of the hard B deposit at three locations at 300X and 3000X magnification. The hard B deposit at the metal deposit interface reveals that the particles comprising the innermost layer show much greater signs of having reacted with other constituents. The spheroids were distorted and had a frosted appearance. Particles of fly ash at

the outer surface exhibit some perfect spheroids of clear, unreacted material. Figures 26 through 29 represent the wavelength dispersive X-ray chart of the hard B deposit. The major elements S, Cl, Fe, Zn, and Pb were detected. The lead was concentrated on the outer surface of the deposit.

X-ray diffraction analysis using the diffractometric technique was conducted to determine the phases present of the two deposit types. The X-ray diffraction parameters are given in Table 8. The soft A deposit was composed primarily of  $\text{CaSO}_4$  and  $\text{Ca}_2\text{Al}_2\text{SiO}_7$ ; other minor phases were identified as NaCl and KCl. The hard B deposit was composed primarily of hematite ( $\text{Fe}_2\text{O}_3$ ) and  $\text{CaSO}_4$ ; other minor phases were identified as NaCl and KCl. The X-ray diffraction analysis failed to identify any Zn or Pb compounds caused by low concentration on superimposition with other phases. Photographs of the X-ray diffraction chart are shown in Figure 30.

The results of the metallurgical and chemical analyses of the superheater tubes indicate that the samples contained a high level of NaCl and KCl, as well as  $\text{CaSO}_4$ . Some Zn and Pb were detected by chemical analysis, but the X-ray diffraction analysis failed to detect any Zn or Pb compounds caused by superimposition with other diffraction lines. The light-colored A deposit was primarily composed of  $\text{CaSO}_4$  and calcium aluminum silicate ( $\text{Ca}_2\text{Al}_2\text{SiO}_7$ ) with a pH of 6.9, which indicates the neutrality of the deposit. The hard, dark-colored B deposit was primarily composed of iron oxide ( $\text{Fe}_2\text{O}_3$ ) and some secondary phases of NaCl and KCl and  $\text{CaSO}_4$ . The pH analysis of the dark B deposit indicates a 3.8 pH level, confirming the belief that sufficient quantities of acid ( $\text{HCl}$ ,  $\text{H}_2\text{SO}_4$ ) or hygroscopic salts are present in the deposit. In a refuse-fired steam generator the downtime period can be a critical stage to form hygroscopic salts on the tube surface if the gas-stream temperature cools below the dew point of the  $\text{HCl}$  or  $\text{H}_2\text{SO}_4$ . Accelerated corrosion often approaches catastrophic proportions when alkali metal chlorides, as well as heavy metal oxides or chlorides with low-melting sulfur-bearing compounds, are present.

## CONCLUSIONS

Review of the literature, laboratory experiments, and field data suggest that fouling is probably due to the presence of alkalis in the refuse. Therefore, the furnace exit temperature should not be allowed to exceed 1800 to 1850°F (982 to 1010°C). It is recommended that the total alkali ( $\text{Na}_2\text{O} + \text{K}_2\text{O}$ , calculated as  $\text{Na}_2\text{O}$ ) not exceed 0.4 percent by weight on a dry-fuel basis. Metal temperatures should not exceed 900 to 950°F (482 to 510°C).

Corrosion occurs at metal temperatures over 950°F (510°C) under oxidizing conditions and about 680 to 700°F (360 to 371°C) under reducing conditions in the presence of ash. Although the mechanisms are not fully understood, they apparently depend on the presence of alkalis

and the heavy metals zinc and lead. It appears doubtful that corrosion is due to pyrosulfates or complex alkali from iron sulfates. The influence of the chlorides under oxidizing conditions is questionable.

Although refuse is a heterogeneous fuel, the problems appear to be similar in many steam generators. Differences are probably due to variations in internal environmental conditions and operational parameters and the occasional absence of corrosion-causing elements.

Not all experiences, however, are unfavorable. Others show that improved steam generator design and controlled operational procedures can be effectively applied to minimize the potential corrosion and deposit phenomenon attributed to refuse.

1. J. L. G. DeLort et al., "The Role of Chloride in the Corrosion Caused by Fly Ashes and Their Deposits," Transactions of the Institution of Mechanical Engineers, London, Vol. 71, Part 1B, 1961, pp. 30-34.
2. G. B. Cook, "Hydrochloric Acid Deposition in Refuse-Burning Installations," Engineering News-Record, Vol. 48, No. 2, February 1961, pp. 34-35.
3. K. Matsumoto, "Experiments for Clarifying the Causes of Corrosion in Waste-Burning Plants," Energy, Vol. 16, No. 5, August 1961, pp. 332-334.
4. F. Kowalski, "Theoretical Experiments on the Refuse-Burning Plant at Stuttgart," Engineering News-Record, Vol. 48, No. 2, February 1961, pp. 71-76.
5. E. Park, "Corrosion Damage in Waste Incinerators of Refuse-Burning Installations," Energy, Vol. 16, No. 5, August 1961, pp. 335-336.
6. F. Kowalski, "Corrosion Problems in Refuse Burners," Metallurgical Engineering, Vol. 142, No. 6, June 1961, pp. 209-212.
7. F. Kowalski, "The Behavior of Boiler Tube Materials in Gases," Engineering News-Record, Vol. 48, No. 2, February 1961, pp. 78-81.
8. E. Park, "Sulfuric Acid Deposits and Corrosion in Refuse-Burning Plants," Engineering News-Record, Vol. 103, June 1961, pp. 117-118.
9. F. Kowalski, "Corrosion Resistance in the Steam Generation of a Waste-Burning Installation," Energy, Vol. 16, No. 5, August 1961, pp. 337-338.
10. F. Kowalski, "Corrosion Problems in Incinerators," Engineering News-Record, Vol. 48, No. 5, November 1961, pp. 31-33.



## ACKNOWLEDGMENT

The authors wish to thank W.R. Applett, Jr., for reviewing this work. The metallographic analysis of the superheater tubes was conducted by J. Cocubinsky and is gratefully acknowledged.

## REFERENCES

1. R.W. Bryers and Z.E. Kerekes, "Corrosion and Fouling in Refuse-Fired Steam Generators," presented at the Symposium on Solid Waste Disposal, AIChE 70th National Meeting, Atlantic City, New Jersey, August 29-September 1, 1971, Preprint 46-b.
2. F.E. Wisely et al., "Study of Refuse as Supplementary Fuel for Power Plants," Horner and Schifrin, Inc., report to City of St. Louis, Missouri, on Bureau of Solid Waste Management Grant No. 1-DOI-UI-00176-01, March 1970.
3. J.R. Michel and L.S. Wilcoxson, "Ash Deposits on Boiler Surfaces From Burning Central Illinois Coal," ASME Paper No. 55-A-95.
4. A.J.B. Cutler et al., "The Role of Chloride in the Corrosion Caused by Flue Gases and Their Deposits," Transactions of the ASME, Journal of Engineering for Power, Series A, Vol. 93, July 1971, pp. 307-312.
5. R. Huch, "Hydrochloric Acid Corrosion in Refuse-Burning Installations," Brennstoff-Warme-Kraft, Vol. 18, No. 2, February 1969, pp. 76-79.
6. P. Steller, "Experiments for Clarifying the Causes of Corrosion in Refuse-Burning Plants," Energie, Vol. 18, No. 8, August 1966, pp. 355-357.
7. F. Nowark, "Operating Experience at the Refuse-Burning Plant at Stuttgart," Brennstoff-Warme-Kraft, Vol. 19, No. 2, February 1967, pp. 71-76.
8. K. Perl, "Corrosion Damage to Steam Generators of Refuse-Burning Installations," Energie, Vol. 18, No. 8, August 1966, pp. 353-354.
9. F. Nowak, "Corrosion Phenomenon in Refuse Boilers," Mitteilungen der VGB, Vol. 102, No. 6, June 1966, pp. 209-210.
10. F.J. Angened, "The Behavior of Boiler Tube Materials in Gases Containing HCl," Brennstoff-Warme-Kraft, Vol. 18, No. 2, February 1966, pp. 79-81.
11. H. Kohle, "Fireside Deposits and Corrosion in Refuse-Burning Boilers," Mitteilungen der VGB, Vol. 102, June 1966, pp. 177-179.
12. P. Steller, "Corrosion Measurements in the Steam Generator of a Refuse-Burning Installation," Energie, Vol. 19, No. 9, September 1967, pp. 278-280.
13. F. Nowak, "Corrosion Problems in Incinerators," Combustion, Vol. 40, No. 5, November 1968, pp. 32-40.

14. F. Nowark, "Corrosion Phenomena in Refuse-Burning Boilers and Preventive Measures," presented at VGB International Symposium on Corrosion in Refuse Incineration Plants, Dusseldorf, Germany, April 1970.
15. H. Hilsheimer, "Experience after 20,000 Operating Hours: the Mannheim Incinerator," Proceedings of the 1970 Refuse Incinerator Conference, ASME, pp. 93-106.
16. F. Maikranz, "Corrosion in Three Different Firing Installations," presented at VGB International Symposium on Corrosion in Refuse Incineration Plants, Dusseldorf, Germany, 1970.
17. K.H. Thomen, "Contribution to the Control of Corrosion Problems on Incinerators With Waterwall Steam Generators," Proceedings of the 1972 National Incinerator Conference, ASME, pp. 310-318.
18. K. Fassler, H. Leib, and H. Spann, "Corrosion in Refuse-Burning Boilers," Mitteilungen der VGB, Vol. 48, No. 2, April 1968, pp. 126-139.
19. C. Cain and W. Nelson, "Corrosion of Superheaters and Reheaters of Pulverized-Coal-Fired Boilers, II," Transactions of the ASME, Journal of Engineering for Power, Series A, Vol. 83, 1961, pp. 468-474.
20. W. Nelson and C. Cain, "Corrosion of Superheaters and Reheaters of Pulverized-Coal-Fired Boilers," Transactions of the ASME, Journal of Engineering for Power, Series A, Vol. 82, 1960, pp. 194-204.
21. R.W. Bryers and Z.E. Kerekes, "Recent Experience With Ash Deposits in Refuse-Fired Boilers," ASME Paper No. 68-WA/CD-4.
22. R.W. Bryers and Z.E. Kerekes, "A Survey of Ash Deposits and Corrosion in Refuse-Fired Boilers," presented at VGB International Symposium on Corrosion in Refuse Incinerator Plants, Dusseldorf, Germany, April 1970, pp. 34-41.
23. J. Defeche, "Corrosions Caused by the Incineration of Urban Residue," report composed by Work Group 3, 4th International Congress of G.E.R.O.M., June 5, 1969.

TABLE 1. COMPARISON OF DEPOSIT ANALYSES  
FROM VARIOUS DOMESTIC AND EUROPEAN INCINERATORS

Constituent	Norfolk (Conv. Pass)	Oceanside (Conv. Pass)	Miami, Ohio (Conv. Pass)	Stuttgart (Furnace) (Supht.)	Munich (Furnace) (Supht.)	Düsseldorf (Furnace) (Supht.)	Essen (Furnace)
SiO <sub>2</sub>	36.5	6.00	5.3	24.0	12.0	20.0	52.54
Al <sub>2</sub> O <sub>3</sub>	17.5	4.00	9.4	11.0	5.0	14.0	22.47
Fe <sub>2</sub> O <sub>3</sub>	12.0	18.0	10.7	12.5	24.0	5.5	12.04
CaO	10.0	1.80	1.4	11.0	9.0	8.8	8.20
MgO	0.9	0.90	-	2.21	1.59	1.99	1.19
Na <sub>2</sub> O	3.51	5.12	10.1	0.08	2.97	3.99	1.81
K <sub>2</sub> O	3.0	13.0	18.1	5.58	8.97	8.27	3.18
PbO	0.67	5.12	10.8	2.69	4.96	5.92	-
ZnO	7.44	9.65	9.3	4.97	4.99	8.09	-
P <sub>2</sub> O <sub>5</sub>	1.71	0.60	-	NIL	1.14	0.5	1.05
TiO <sub>2</sub>	2.00	0.50	-	1.05	0.4	0.75	0.91
SO <sub>3</sub>	8.4	26.1	20.6	18.86	21.71	30.49	0.14
Cl	0.2	1.58	1.0	NIL	NIL	NIL	NIL

(All analyses in percent by weight)

TABLE 2 ASH ANALYSES AND FUSION TEMPERATURES  
OF MUNICIPAL REFUSE COMPONENTS AND SLAGS

ASTM Fusion Temp. °F *	Clear Glass	Brown Glass	Green Glass	Garbage, less bones	Card-board, corrug.	Misc. Paper (1)	Grass and dirt	Textiles	Heavy plastics, leather, etc.	Bones & clam shells
Initial Softening Fluid	1620	1700	2080	2100	2120	2260	2200	2120	2160	2800
	74.11	71.86	75.21	46.35	47.92	48.27	61.50	38.85	34.18	63.40
Silica	4.97	7.21	9.42	4.29	6.97	7.02	6.98	5.71	6.22	0.84
Alumina	9.36	11.70	8.62	20.70	18.08	11.70	12.87	23.65	31.04	23.90
Calcium oxide	0.09	0.04	0.03	2.86	4.28	3.21	1.69	3.14	2.09	0.98
Ferric oxide	Tr	Tr	Tr	1.04	7.21	8.69	1.83	0.62	9.23	Tr
Titania	8.16	0.43	0.02	11.06	9.62	8.94	7.61	9.34	8.71	4.28
Magnesia	0.07	0.08	0.11	0.0?	0.41	0.03	0.37	0.07	0.04	0.09
Barium oxide	2.09	6.02	4.31	5.01	3.26	5.72	2.09	3.84	4.19	0.70
Soda	0.05	0.82	0.74	5.16	0.27	4.29	1.14	5.16	1.04	0.04
Potash	0.03	0.02	0.04	0.32	0.39	0.41	0.53	0.01	1.84	0.02
Zinc oxide	0.09	0.08	0.06	2.02	0.14	0.39	2.28	0.06	0.06	3.75
Phos. pentoxide	0.14	0.27	0.18	0.21	0.12	0.14	0.08	0.37	0.16	0.32
Sulfur trioxide										
TOTALS	99.16	98.53	98.74	99.04	98.67	98.81	98.97	98.82	98.80	98.32

\*Conversion factor: °C = 5/9(°F - 32)

TABLE 2 ASH ANALYSES AND FUSION TEMPERATURES  
OF MUNICIPAL REFUSE COMPONENTS AND SLAGS (CONT)

	Slag C (2) Contin. Feed	Slag F (2) Batch Feed	Avg. 25 Slags (2)	Herbert Slags (3)	Suspended in Hot Flue Gas	Dust		Stack
						Collector Zone	Stack	
SiO <sub>2</sub>	37.1	20.9	44.73	46.3	47.2	48.7	36.5	SiO <sub>2</sub>
Al <sub>2</sub> O <sub>3</sub>	7.0	15.2	17.44	18.35	10.2	23.4	25.9	Al <sub>2</sub> O <sub>3</sub>
CaO	7.7	12.7	10.52	9.94	18.4	9.2	8.9	CaO
Fe <sub>2</sub> O <sub>3</sub>	40.0	1.8	9.26	8.85	15.6	6.5	7.1	Fe <sub>2</sub> O <sub>3</sub>
TiO <sub>2</sub>	0.55	2.4	2.92	2.90	-	1.1	0.7	TiO <sub>2</sub>
MgO	1.2	2.4	2.1	2.54	2.9	2.3	2.8	MgO
BaO	Tr	Tr	Tr	0.58	-	-	-	BaO
Na <sub>2</sub> O	5.36	17.23	8.14	4.61	4.5	5.8	10.5	Na <sub>2</sub> O
K <sub>2</sub> O								K <sub>2</sub> O
ZnO	0.20	6.3	* 1.54	1.37	-	-	-	ZnO
P <sub>2</sub> O <sub>5</sub>	0.6	0.7	1.52	2.15	-	-	-	P <sub>2</sub> O <sub>5</sub>
SO <sub>3</sub>	0.55	20.4	* 3.69	** 0.96	1.2	3.0	7.6	SO <sub>3</sub>
MnO <sub>2</sub>	0.30	0.44	0.29	-	-	-	-	MnO <sub>2</sub>
CuO	-	0.3	Tr	-	-	-	-	CuO
PbO	-	0.2	Tr	-	-	-	-	PbO
TOTALS	100.56	100.97	102.15	98.55	100.0	100.0	100.0	

(1) All paper except newspaper and corrugated cardboard, some smeared with garbage

(2) G. H. Criss and A. R. Olsen, "The Chemistry of Incinerator Slags and Their Compatibility with Fire Clay and Alumina Refractories," Proceedings of the 1968 National Incinerator Conference, ASME, pp. 53-60.

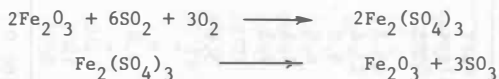
(3) D. B. Herbert, "The Nature of Incinerator Slags," Proceedings of the 1966 National Incinerator Conference, ASME, pp. 191-194.

(4) Elmer Kaiser, "The Sulfur Balance of Incinerators," presented at the Air Pollution Control Association Annual Meeting, June 11-16, 1967, Paper 67-160.

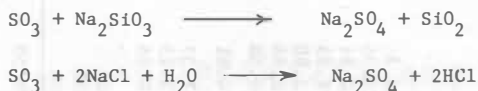
\* 6 samples  
\*\* 2 samples  
Tr Trace

TABLE 3 DEFECHÉ'S PROPOSED REACTIONS

Defeche suggests that the tube surfaces act as a catalyst, forming  $\text{SO}_3$  in the presence of  $\text{SO}_2$  with the formation of ferric sulfate as an intermediate compound:



A part of this sulfuric anhydride ( $\text{SO}_3$ ) reacts with the alkaline silicates and sodium chloride of the deposits to form alkaline sulfate.



The silicates are a product of the reaction of alkaline chlorides with silica.



The sulfuric anhydride ( $\text{SO}_3$ ) reacts also with the alkaline sulfates to yield pyrosulfates which attack the ferric oxide protecting the tube surface, yielding an alkaline sulfate of iron which is then decomposed, resulting in a cyclic process. The overall reaction may be summarized as follows:

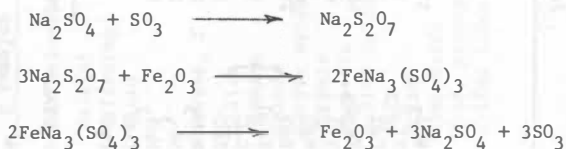


TABLE 3 DEFECHE'S PROPOSED REACTIONS (CONT)

In addition to the attack by the alkaline sulfates, Defeche postulates the direct attack of iron by the oxides of sulfur, e.g.:



He also points out the possibility of sulfite formation through the reduction reactions of carbon and carbon monoxide:



These sulfites are very unstable and decompose to yield the extremely corrosive sodium sulfide according to the reaction:



The  $\text{Na}_2\text{S}$  can react with silicon oxide to form a sulfide of silicon that is equally corrosive:

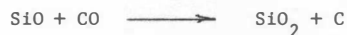




TABLE 4 DESIGN AND OPERATIONAL DATA OF  
A RECENT EUROPEAN REFUSE-FIRED STEAM GENERATOR

Steam Pressure	570 lb/in <sup>2</sup> (4.03 MPa)
Firing rate (100% refuse)	840 U.S. tons/d (762 metric tons)
Flue gas temperature:	
Combustion chamber	1560°F (849°C)
Superheater (1st pass)	1360°F (738°C)
Superheater (2nd pass)	1060°F (571°C)
Tube Metal Temperature:	
Superheater (1st pass):	
Design	770°F (410°C)
Operation	914°F (490°C)

TABLE 5 CHEMICAL COMPOSITION OF DEPOSIT  
FROM SUPERHEATER TUBE

<u>Element</u>	<u>% by Weight</u>	<u>Oxide Form</u>	<u>% by Weight</u>
Si	0.86	SiO <sub>2</sub>	1.83
Al	0.50	Al <sub>2</sub> O <sub>3</sub>	0.94
Ti	0.15	TiO <sub>2</sub>	0.25
Fe	36.26	Fe <sub>2</sub> O <sub>3</sub>	51.85
Ca	1.14	CaO	1.59
Mg	0.2	MgO	0.33
Na	5.71	Na <sub>2</sub> O	7.7
K	9.59	K <sub>2</sub> O	11.56
S	6.3	SO <sub>3</sub>	15.75
P	0.20	P <sub>2</sub> O <sub>5</sub>	0.46
Cl	5.63	Moisture	2.7
		pH	3.5

TABLE 6 ANALYSIS OF FLY ASH  
FROM ELECTROSTATIC PRECIPITATOR

<u>Element</u>	<u>% by Weight</u>	<u>Oxide Form</u>	<u>% by Weight</u>
Si	5.4	SiO <sub>2</sub>	11.6
Ca	8.6	CaO	12.0
Mg	0.6	MgO	1.0
Fe	2.0	Fe <sub>2</sub> O <sub>3</sub>	2.8
Al	6.4	Al <sub>2</sub> O <sub>3</sub>	12.0
Na	7.9	Na <sub>2</sub> O	10.7
K	10.3	K <sub>2</sub> O	12.4
Pb	2.2	PbO	2.4
Zn	4.5	ZnO	5.6
S	6.4	SO <sub>3</sub>	15.9
Cl	12.2	Cl	12.2
Loss on ignition	12.0		
pH	5.8		

ASH FUSION TEMPERATURE, °F (°C)

	<u>Atmosphere</u>	
	<u>Oxidizing</u>	<u>Reducing</u>
Initial deformation	2360 (1293)	2280 (1249)
Softening temperature (spherical)	2440 (1338)	2300 (1260)
Softening temperature (hemispherical)	2500 (1371)	2360 (1293)
Fluid temperature	2560 (1404)	2900 (1593)

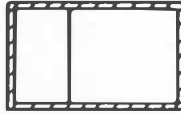
TABLE 7 CHEMICAL COMPOSITION OF DEPOSITS

Soft A				Hard B			
Element	% by Weight	Oxide Form	% by Weight	Element	% by Weight	Oxide Form	% by Weight
Si	6.07	SiO <sub>2</sub>	12.9	Si	1.45	SiO <sub>2</sub>	3.1
Al	5.10	Al <sub>2</sub> O <sub>3</sub>	9.5	Al	2.11	Al <sub>2</sub> O <sub>3</sub>	3.9
Ca	14.56	CaO	20.3	Ca	4.57	CaO	6.4
Mg	2.14	MgO	3.5	Mg	0.57	MgO	0.9
S	8.69	SO <sub>3</sub>	21.7	S	7.23	SO <sub>3</sub>	18.1
P	ND*	-	-	P	ND*	-	-
Fe	1.47	Fe <sub>2</sub> O <sub>3</sub>	2.1	Fe	32.16	Fe <sub>2</sub> O <sub>3</sub>	45.9
Zn	1.94	ZnO	2.4	Zn	1.29	ZnO	1.6
Pb	0.19	PbO	0.2	Pb	0.63	PbO	0.7
Sn	0.19	SnO <sub>2</sub>	0.2	Sn	0.07	SnO <sub>2</sub>	0.09
Cu	0.11	CuO	0.1	Cu	0.10	CuO	0.1
Cl	5.67	Cl	5.67	Cl	6.74	Cl	6.74
Na	3.63	Na <sub>2</sub> O	4.9	Na	2.40	Na <sub>2</sub> O	3.2
K	6.04	K <sub>2</sub> O	7.3	K	6.35	K <sub>2</sub> O	7.7
pH	6.90	-	-	pH	3.80	-	-

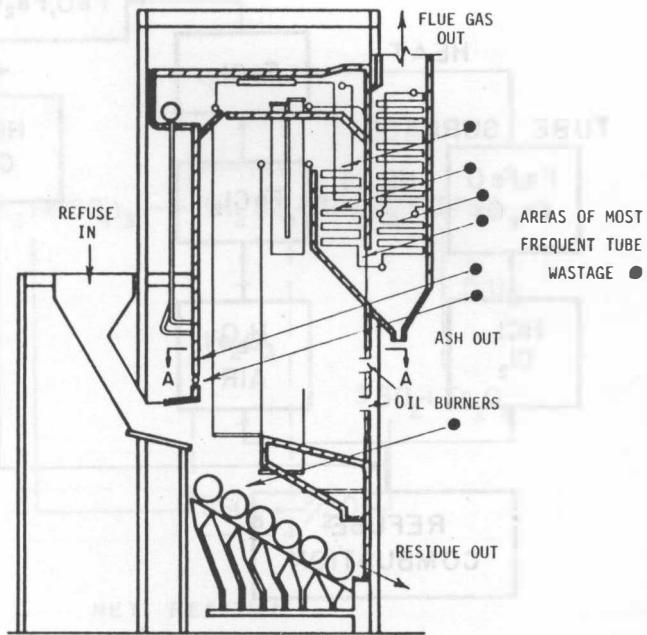
\*Not detectable

TABLE 8 X-RAY DIFFRACTION ANALYSES PARAMETERS

Radiation	Cu
Filter	Ni
Kilovolt	36
Milliampere	20
Chart speed	1 cm/min
Scintillation counter voltage	1125 V
Counts per second	800
Total counts	2



SEC 'A-A'



STUTTGART - MÜNSTER  
UNIT NO. 29

SCALE IN FEET

0 10 20 30 40 50

FIGURE 1 AREAS OF MOST FREQUENT TUBE WASTAGE  
IN THE STUTTGART-MÜNSTER UNITS.

Conversion factor: (ft) = 0.305 (m)

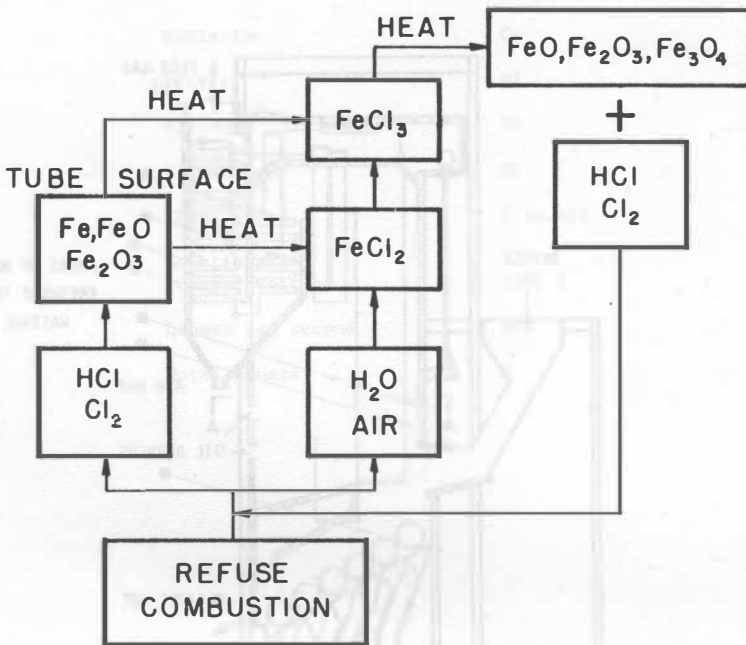


FIGURE 2 CHLORIDE CORROSION FROM FIRING REFUSE AS PROPOSED BY FÄSSLER ET AL.

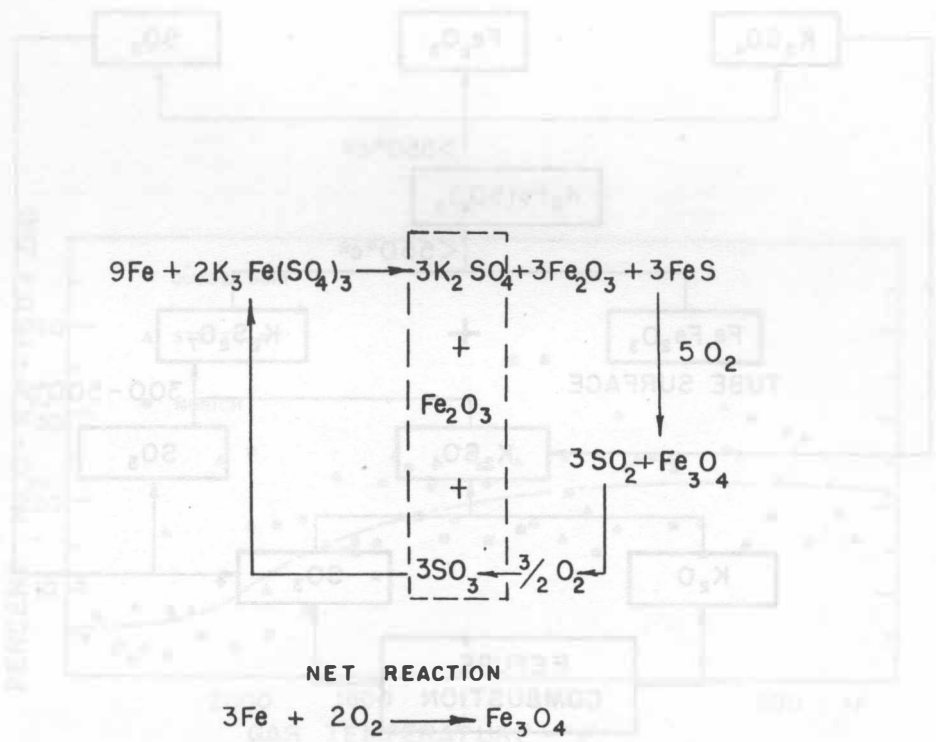


FIGURE 3 COMPLEX ALKALI IRON SULFATE CORROSION MODEL PROPOSED BY CAIN AND NELSON.



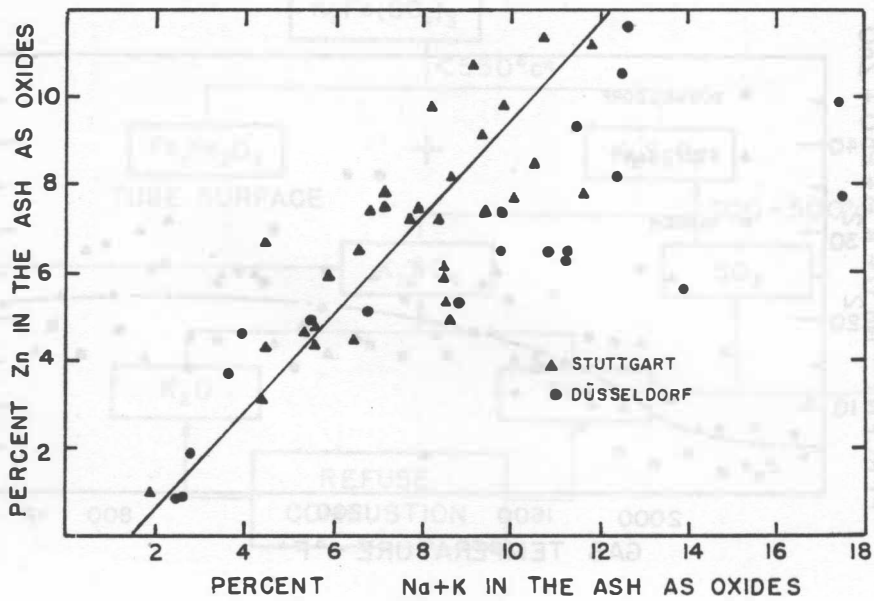


FIGURE 6 RELATIONSHIP OF ZINC CONCENTRATION TO SODIUM AND POTASSIUM CONCENTRATION IN THE ASH.

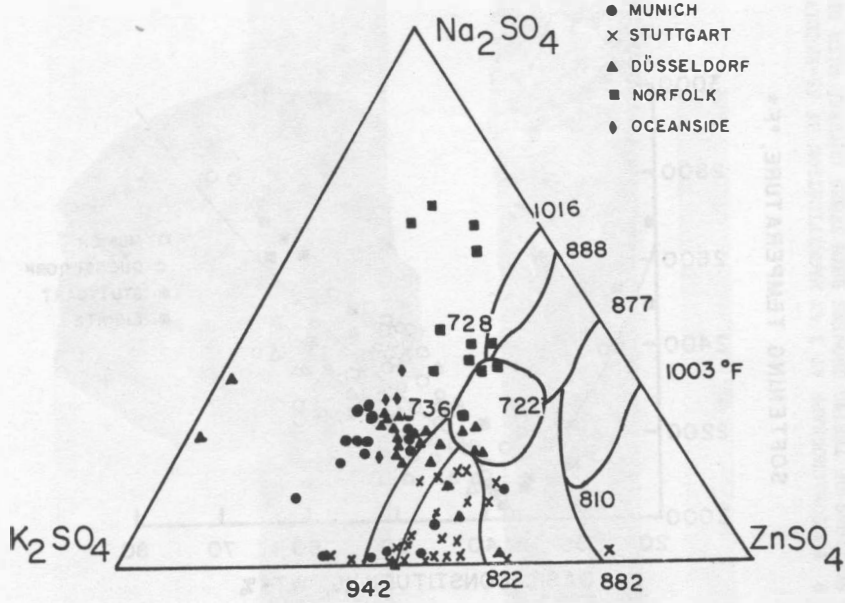


FIGURE 7  $K_2SO_4/Na_2SO_4/ZnSO_4$  PHASE DIAGRAM

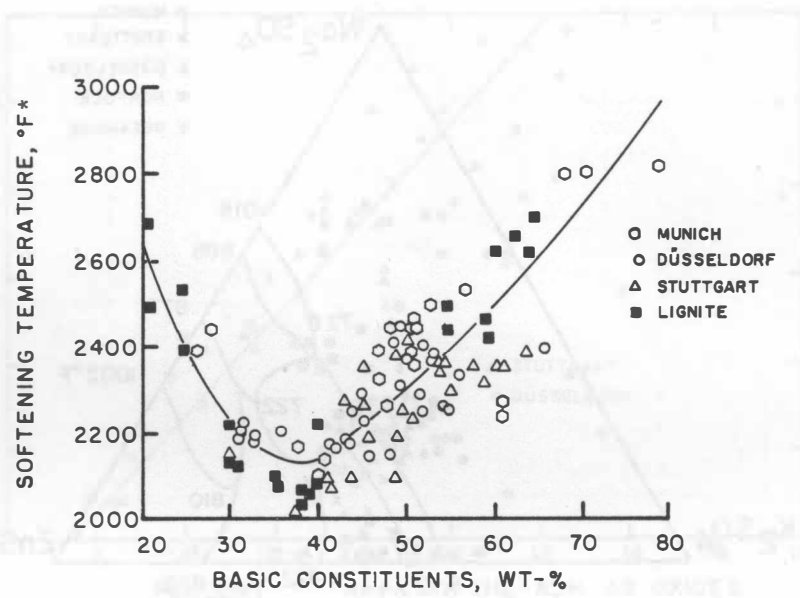


FIGURE 8 SOFTENING TEMPERATURE VERSUS ASH BASE CONTENT.

\*Conversion factor:  $(^{\circ}\text{C}) = 5/9(^{\circ}\text{F} - 32)$

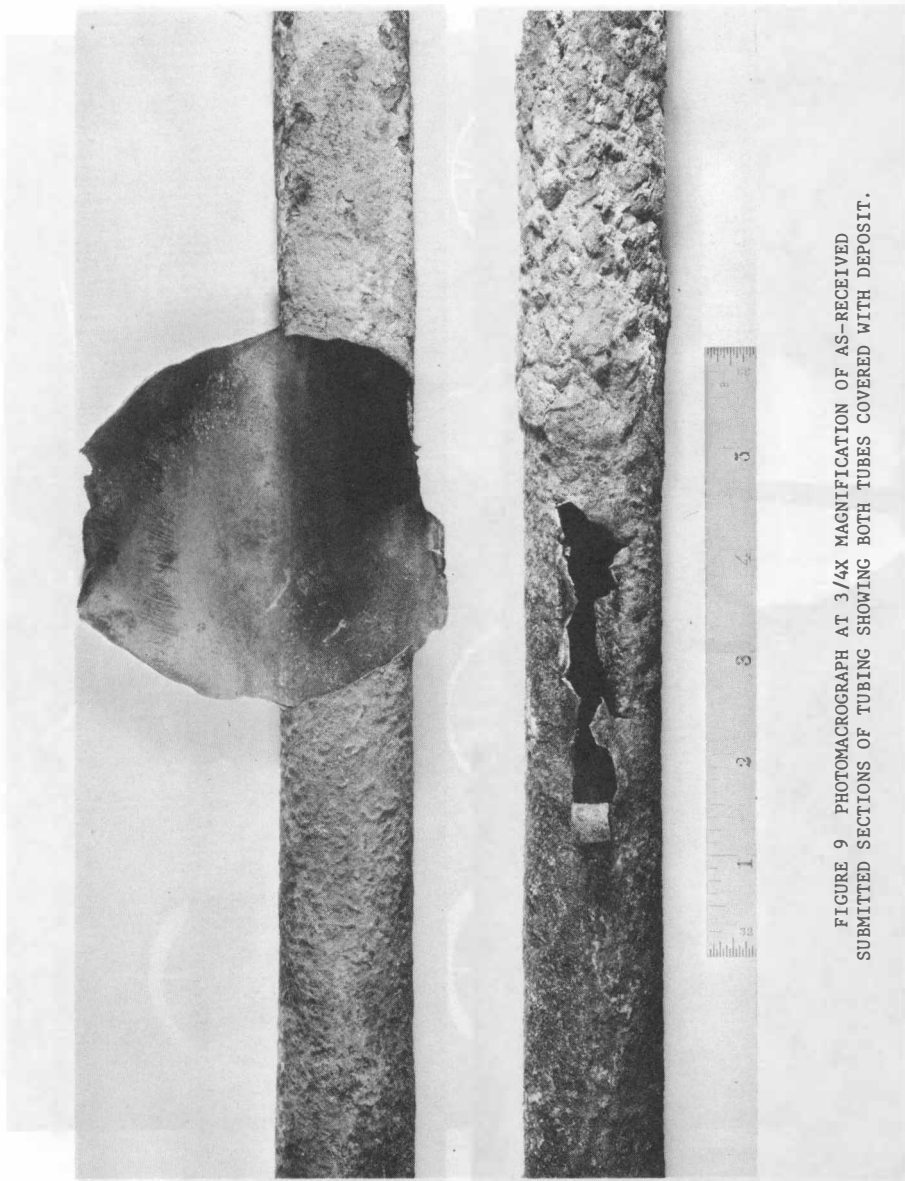


FIGURE 9 PHOTOMICROGRAPH AT 3/4X MAGNIFICATION OF AS-RECEIVED  
SUBMITTED SECTIONS OF TUBING SHOWING BOTH TUBES COVERED WITH DEPOSIT.

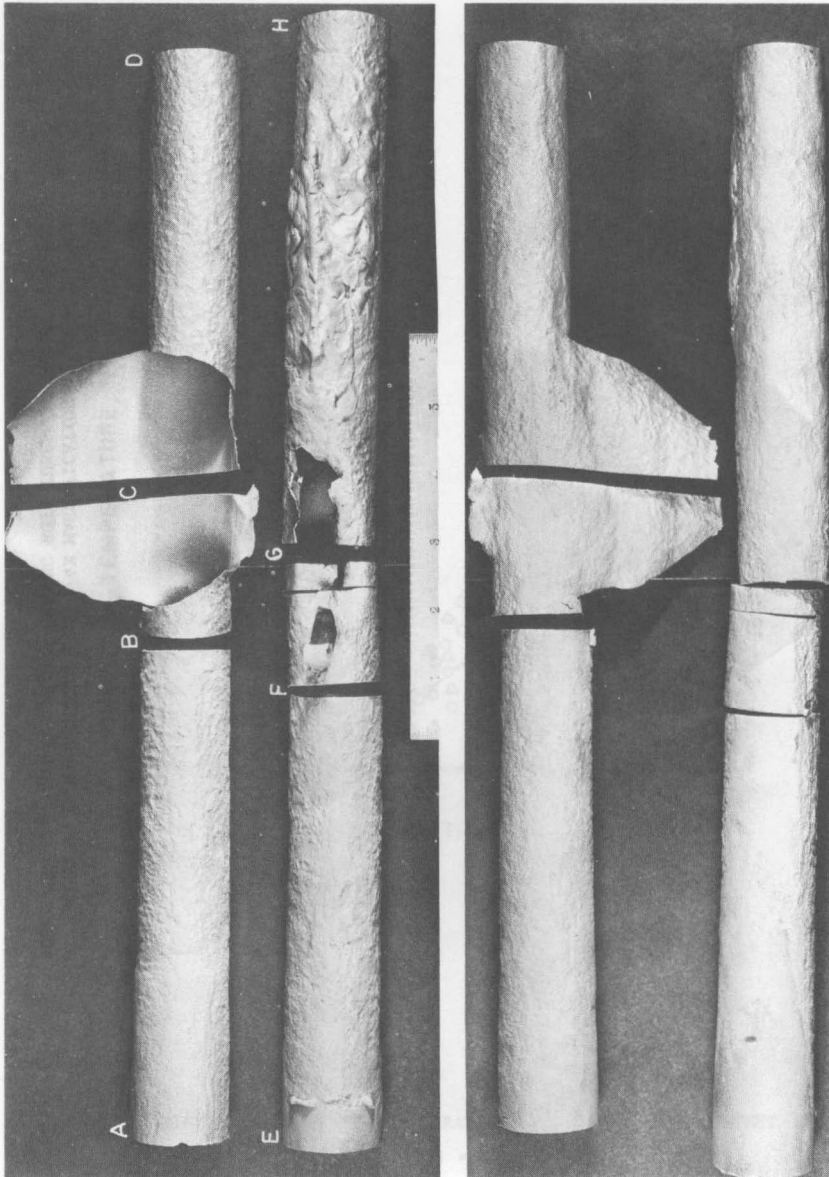


FIGURE 10 PHOTOMICROGRAPH AT 1/2X MAGNIFICATION OF SANDBLASTED TUBES AFTER SURFACES WERE CLEANED. PORTION OF TUBES DIAMETRICALLY OPPOSITE THE FAILURE IS PRESENTED IN BOTTOM PHOTO. TRANSVERSE CROSS SECTIONS REMOVED FOR MICROSCOPIC EXAMINATION ARE IDENTIFIED BY LETTERS.

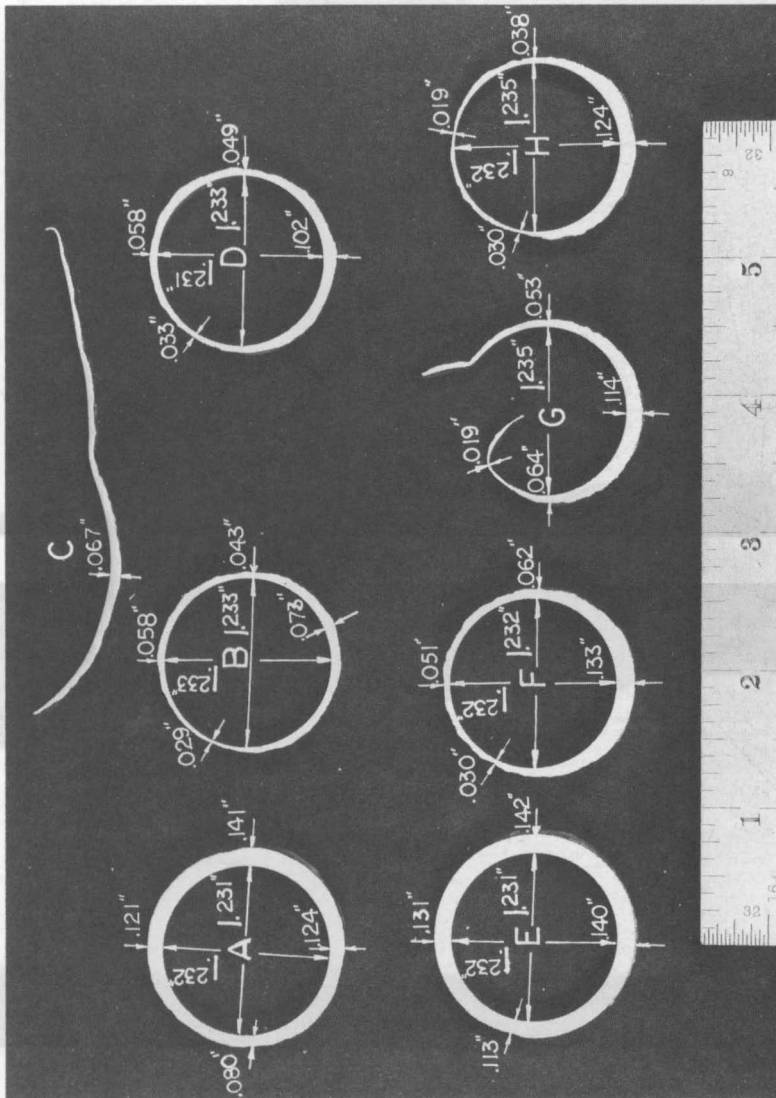


FIGURE 11. PHOTOMICROGRAPH AT 1X MAGNIFICATION OF NITAL ETCHED TRANSVERSE CROSS SECTIONS REMOVED FROM REGIONS SHOWN IN FIGURE 10 WITH INSIDE-DIAMETER AND WALL-THICKNESS MEASUREMENTS.

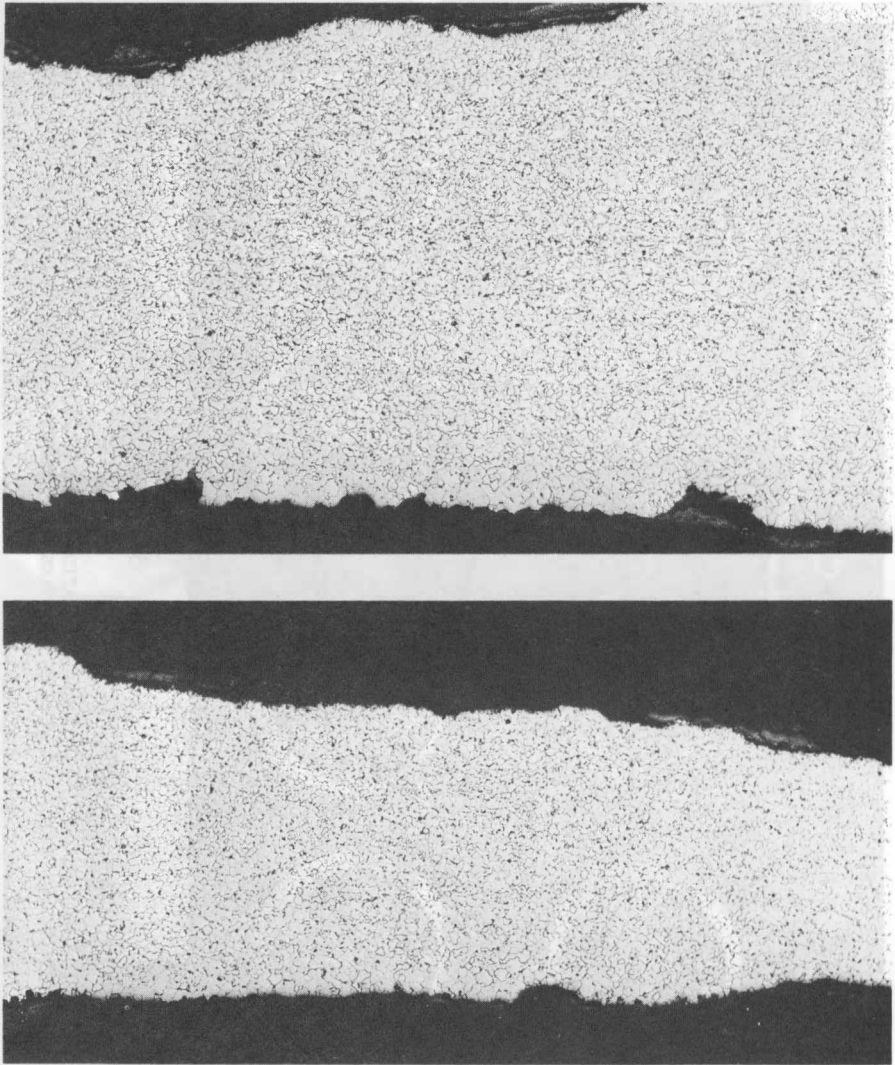


FIGURE 12 PHOTOMICROGRAPHS AT 100X MAGNIFICATION INDICATING REPRESENTATIVE APPEARANCES OF NITAL ETCHED OUTSIDE TUBE SURFACES AT UPPER EDGES OF SECTIONS. THE INSIDE SURFACE (LOWER EDGE) OF TUBES SUFFERED NO SIGNIFICANT ATTACK.

FIGURE 13 X-RAY DIFFRACTION POWDER CAMERA FILM OF FLY ASH (TOP) AND X-RAY DIFFRACTOMETER CHART OF SAME SAMPLE (BOTTOM)

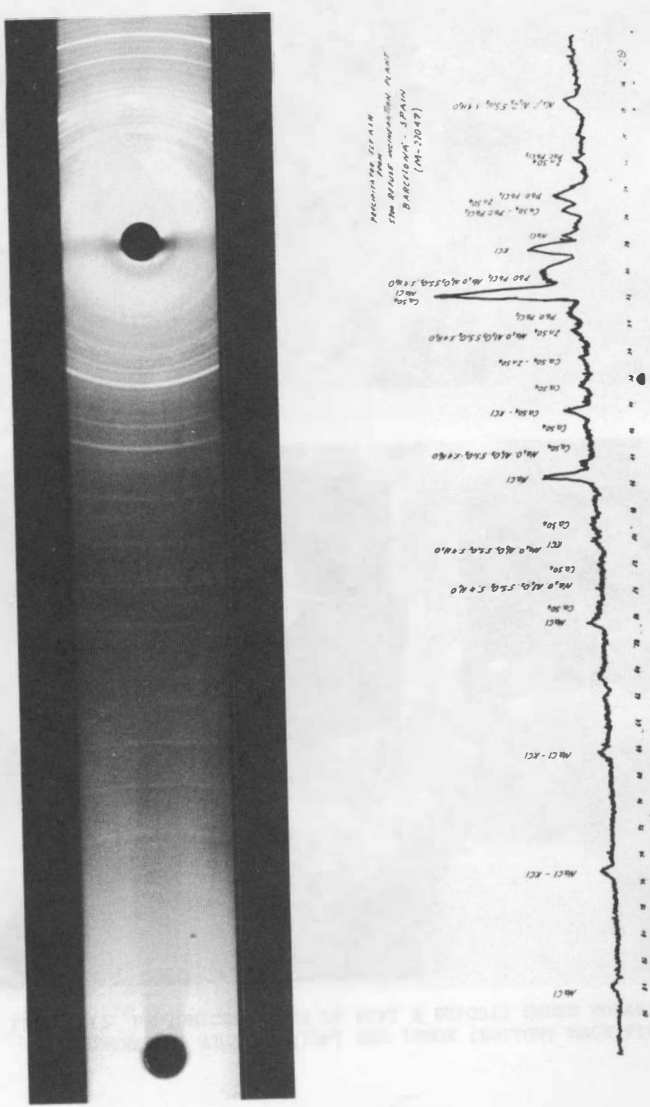


FIGURE 13 X-RAY DIFFRACTION POWDER CAMERA FILM OF FLY ASH (TOP) AND X-RAY DIFFRACTOMETER CHART OF SAME SAMPLE (BOTTOM)



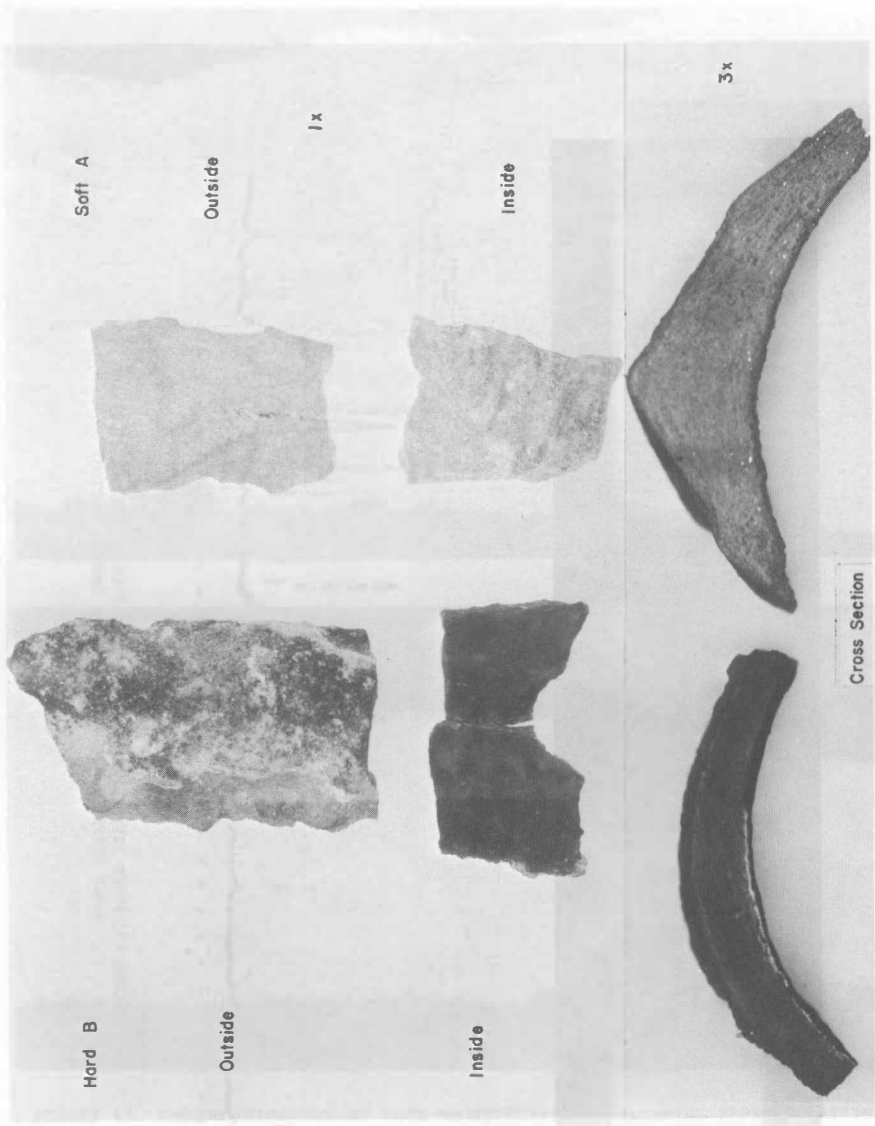


FIGURE 14 AS-RECEIVED DEPOSITS.

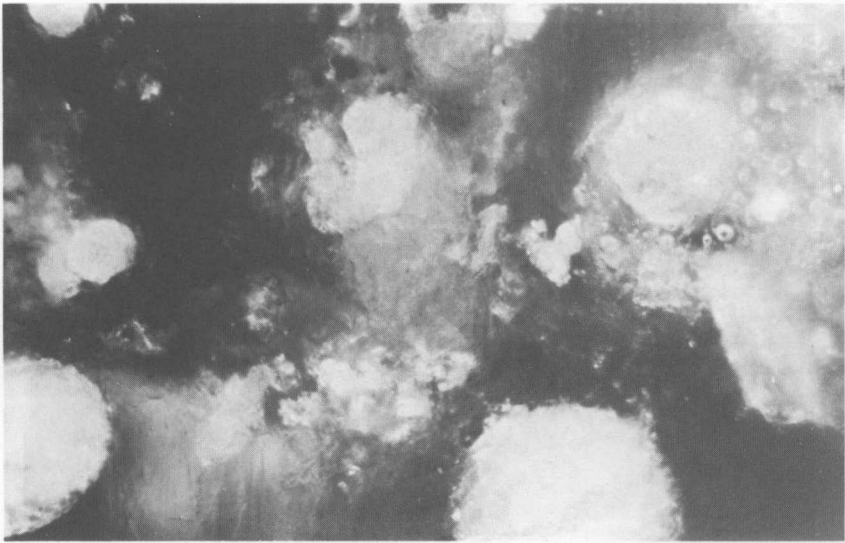
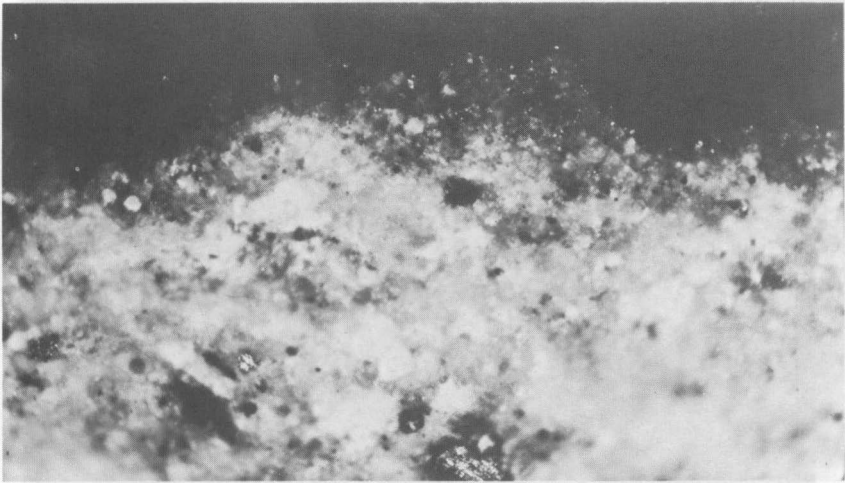


FIGURE 15 PHOTOMICROGRAPHS OF SOFT A DEPOSIT UNDER POLARIZED LIGHT ILLUMINATION AT 100X (TOP) AND 1000X (BOTTOM) MAGNIFICATION.

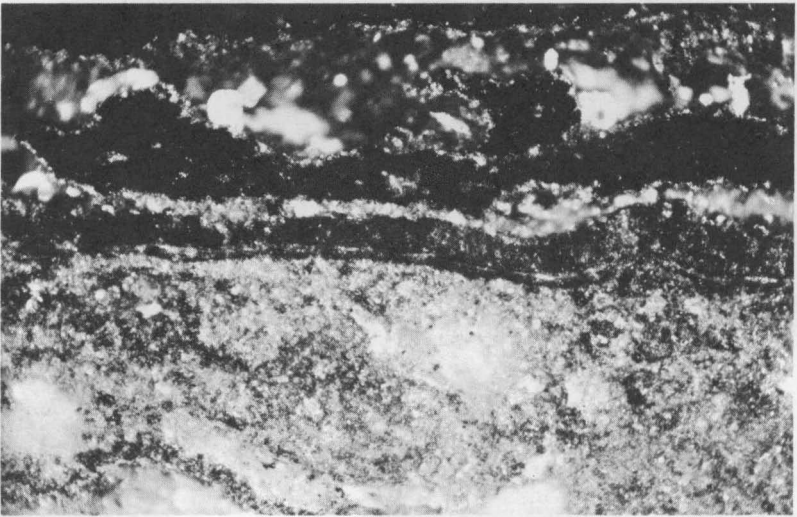
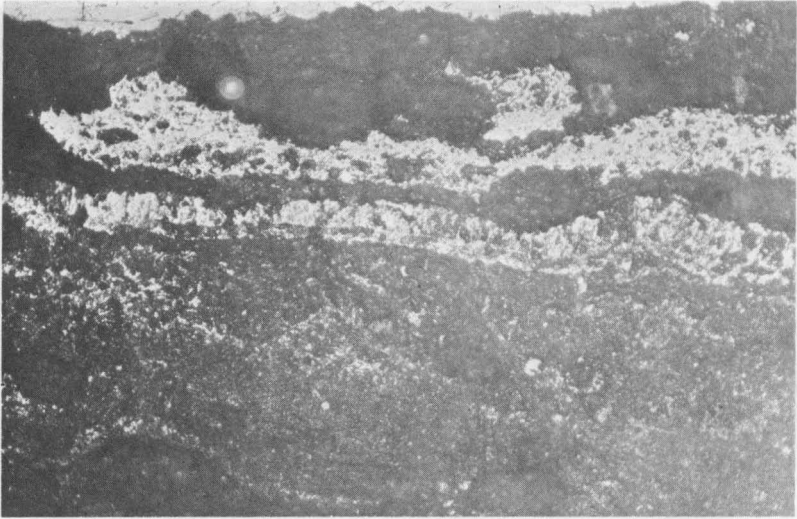


FIGURE 16 PHOTOMICROGRAPHS AT 100X MAGNIFICATION OF HARD B SCALE UNDER WHITE LIGHT ILLUMINATION (TOP) AND POLARIZED LIGHT ILLUMINATION (BOTTOM).

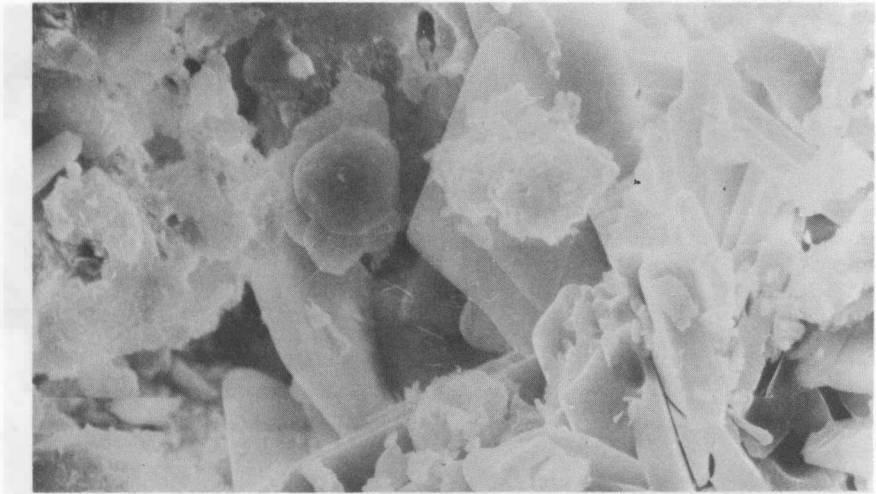
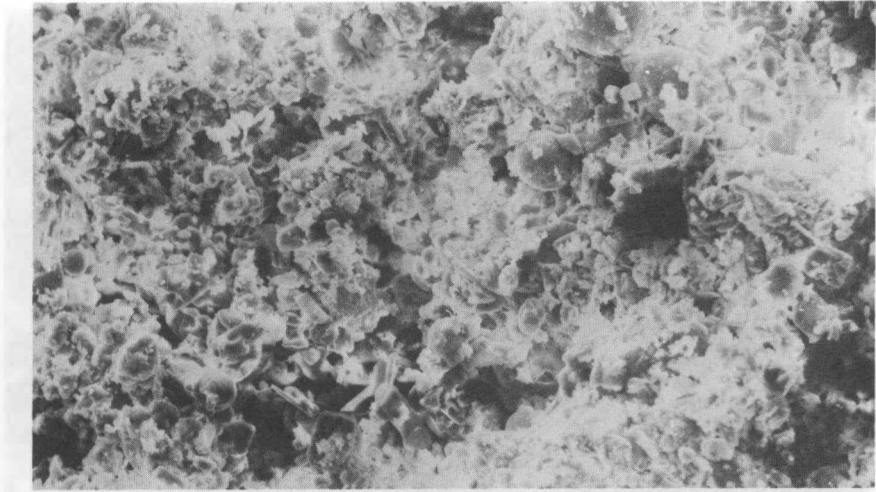


FIGURE 17 SEM PHOTOMICROGRAPHS OF INSIDE SURFACE OF SOFT A DEPOSIT AT 300X (TOP) and 3000X (BOTTOM) MAGNIFICATION.

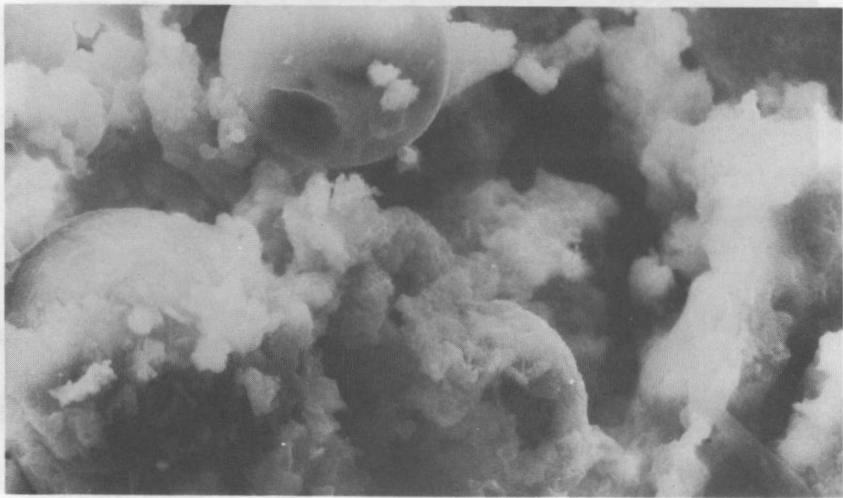
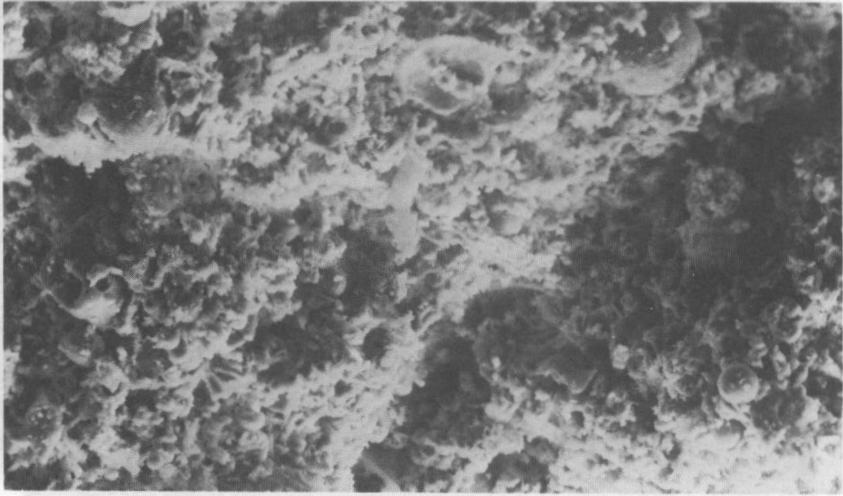


FIGURE 18 SEM PHOTOMICROGRAPHS OF CROSS SECTION OF SOFT A DEPOSIT AT 300X (TOP) AND 3000X (BOTTOM) MAGNIFICATION.

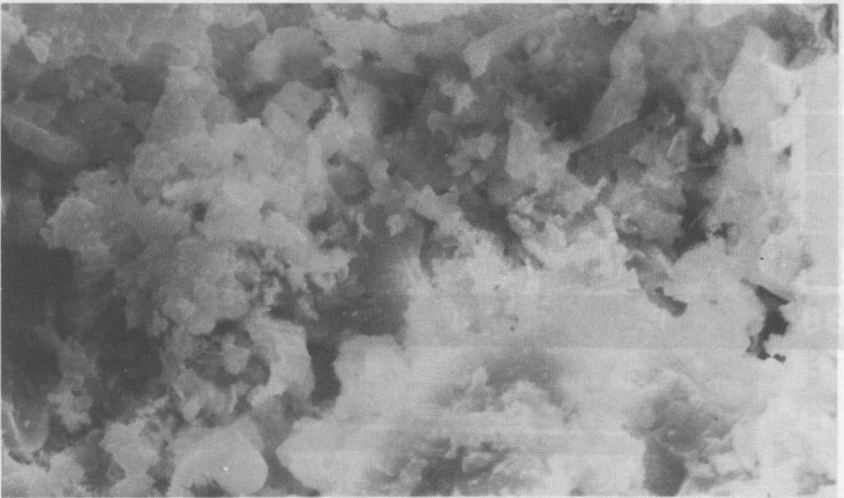
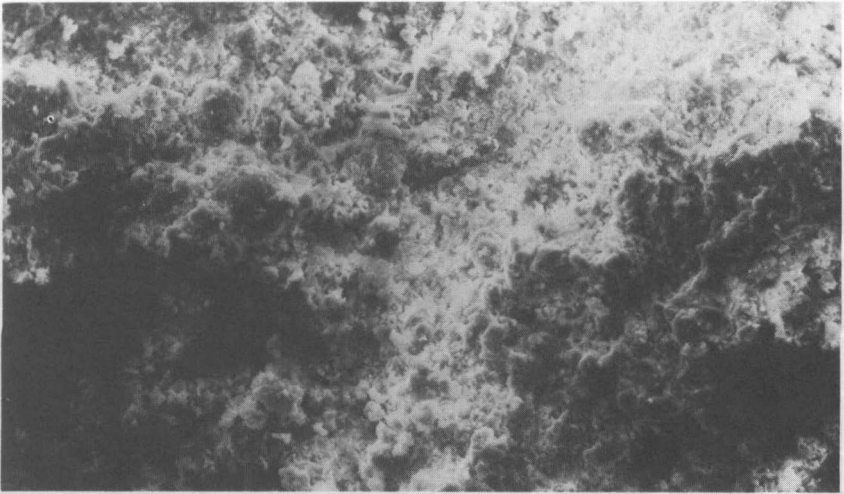


FIGURE 19 SEM PHOTOMICROGRAPHS OF OUTSIDE SURFACE OF SOFT A DEPOSIT AT 300X (TOP) AND 3000X (BOTTOM) MAGNIFICATION.

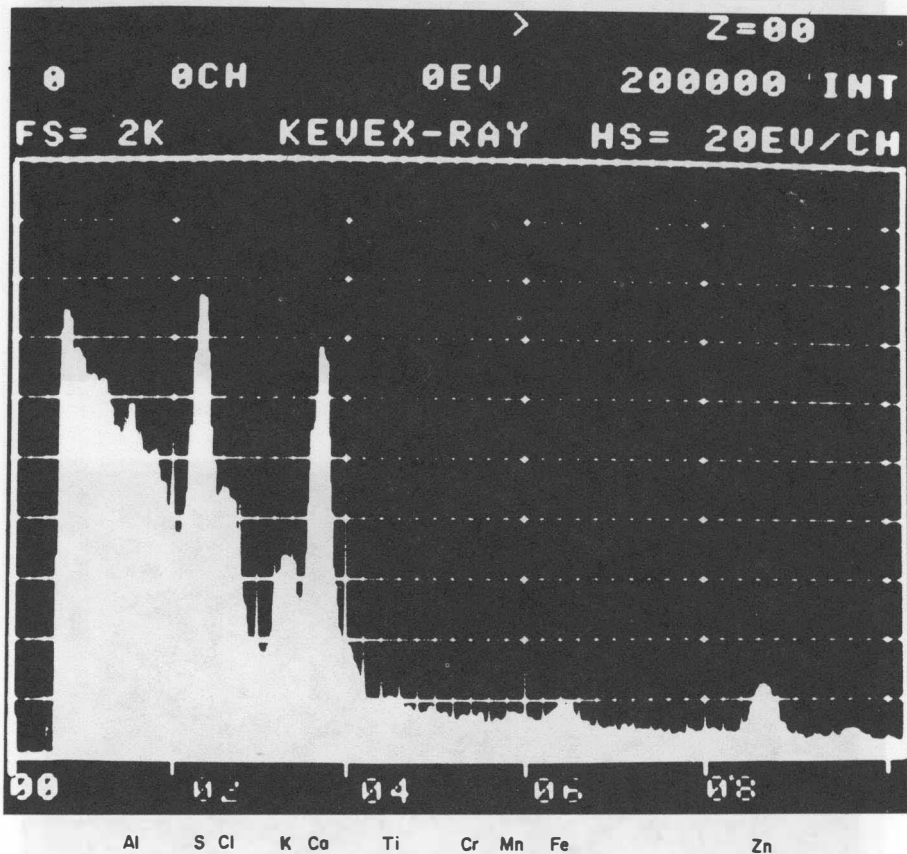


FIGURE 20 WAVELENGTH DISPERSIVE X-RAY ANALYSIS CHART  
OF SOFT A DEPOSIT FROM INSIDE SURFACE AREA.

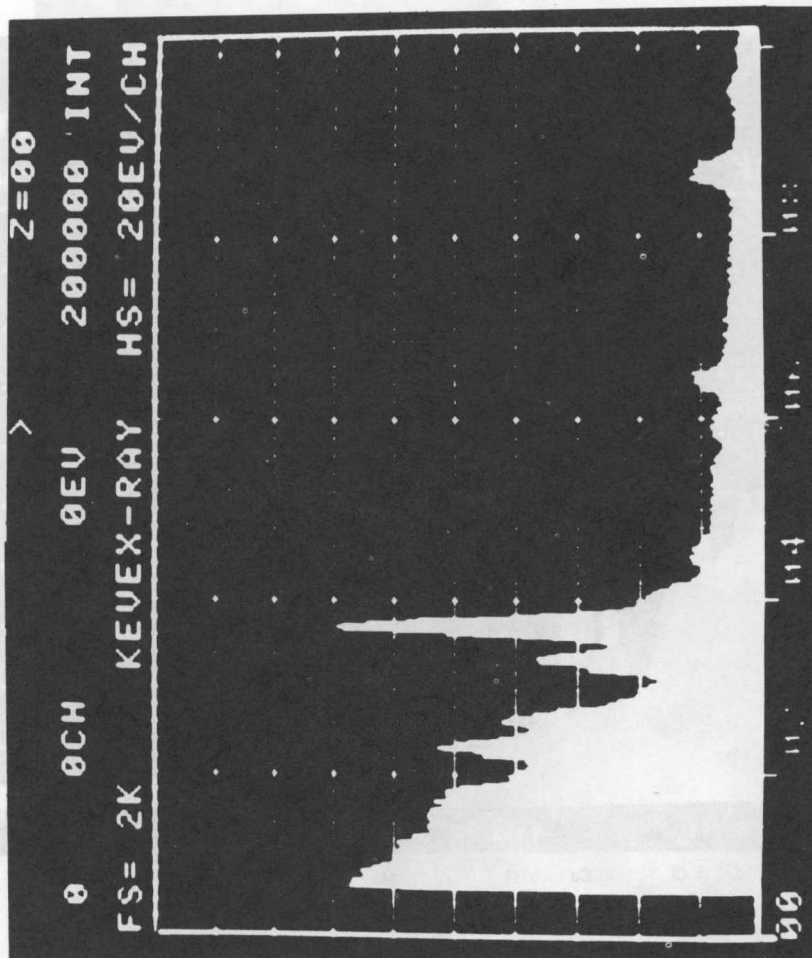


FIGURE 2.1 WAVELENGTH DISPERSIVE X-RAY ANALYSIS CHART OF SOFT A DEPOSIT FROM CROSS-SECTION AREA.



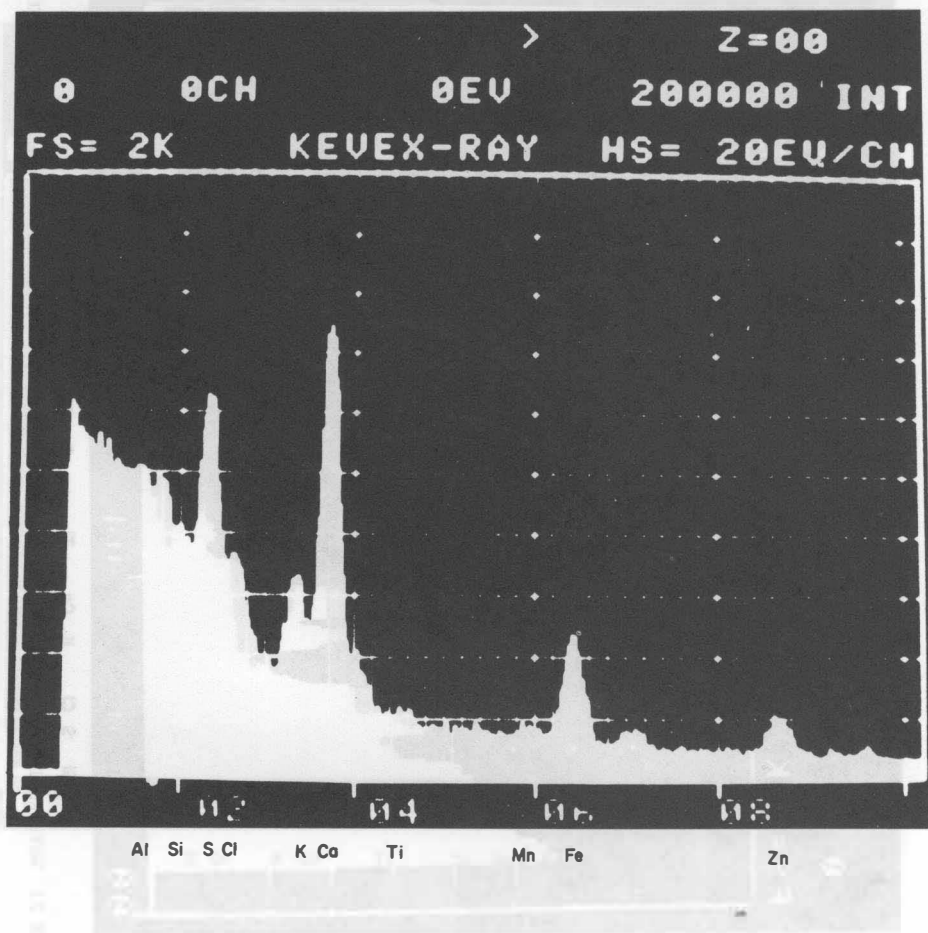


FIGURE 22 WAVELENGTH DISPERSIVE X-RAY ANALYSIS CHART OF SOFT A DEPOSIT FROM OUTSIDE SURFACE AREA.

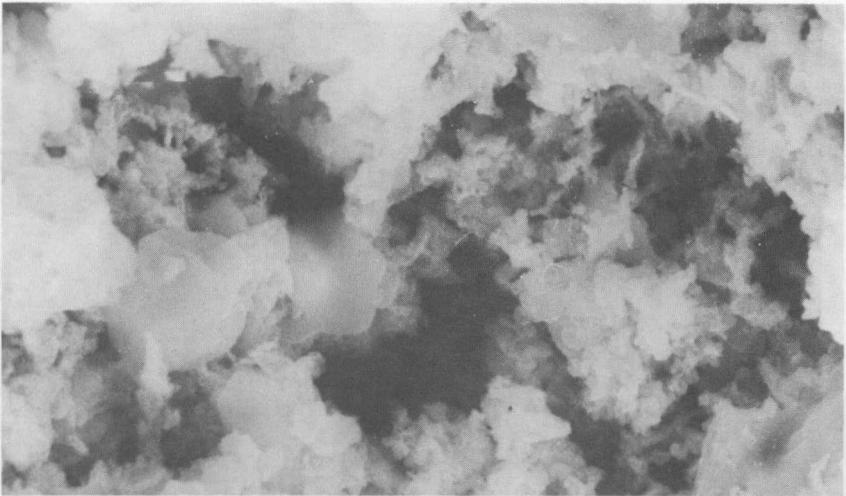
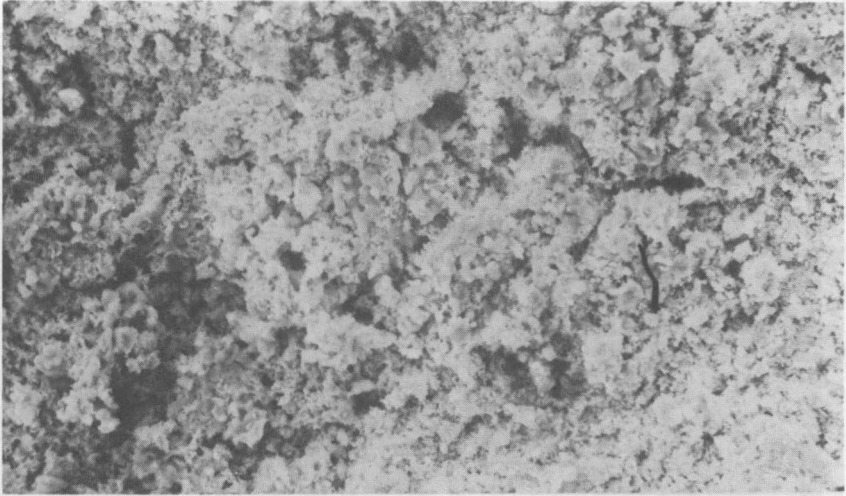


FIGURE 23 SEM PHOTOMICROGRAPHS OF INSIDE SURFACE OF HARD B SCALE AT 300X (TOP) AND 3000X (BOTTOM) MAGNIFICATION.

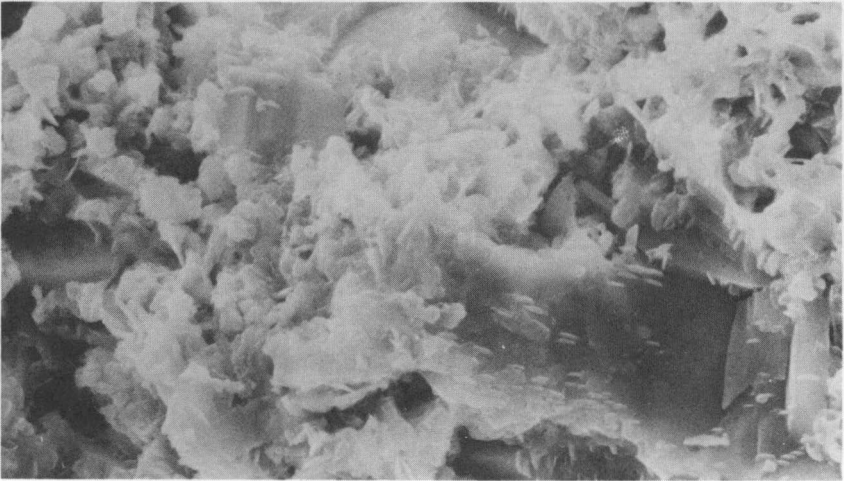
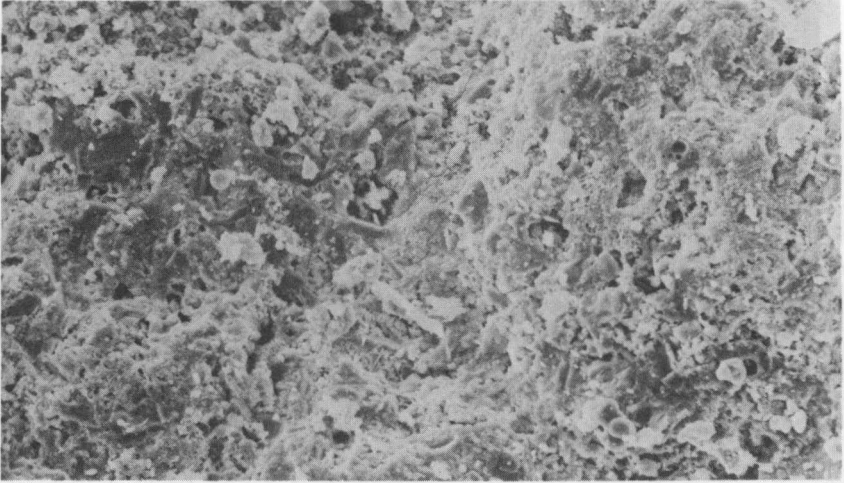


FIGURE 24 SEM PHOTOMICROGRAPHS OF CROSS SECTION OF HARD B SCALE AT 300X (TOP) AND 3000X (BOTTOM) MAGNIFICATION.

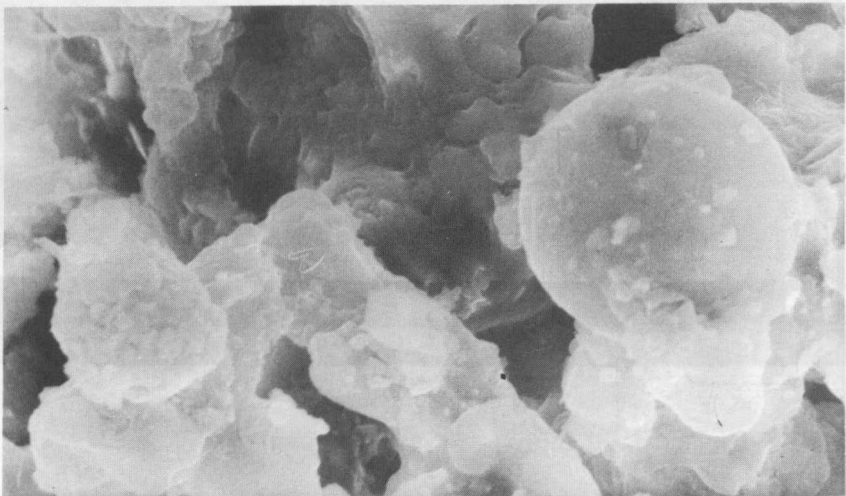
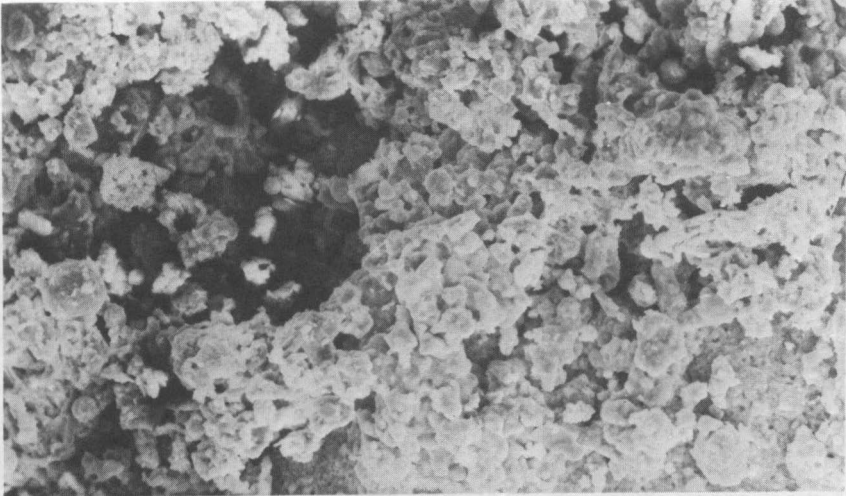


FIGURE 25 SEM PHOTOMICROGRAPHS OF OUTSIDE SURFACE OF HARD B SCALE AT 300X (TOP) AND 3000X (BOTTOM) MAGNIFICATION.

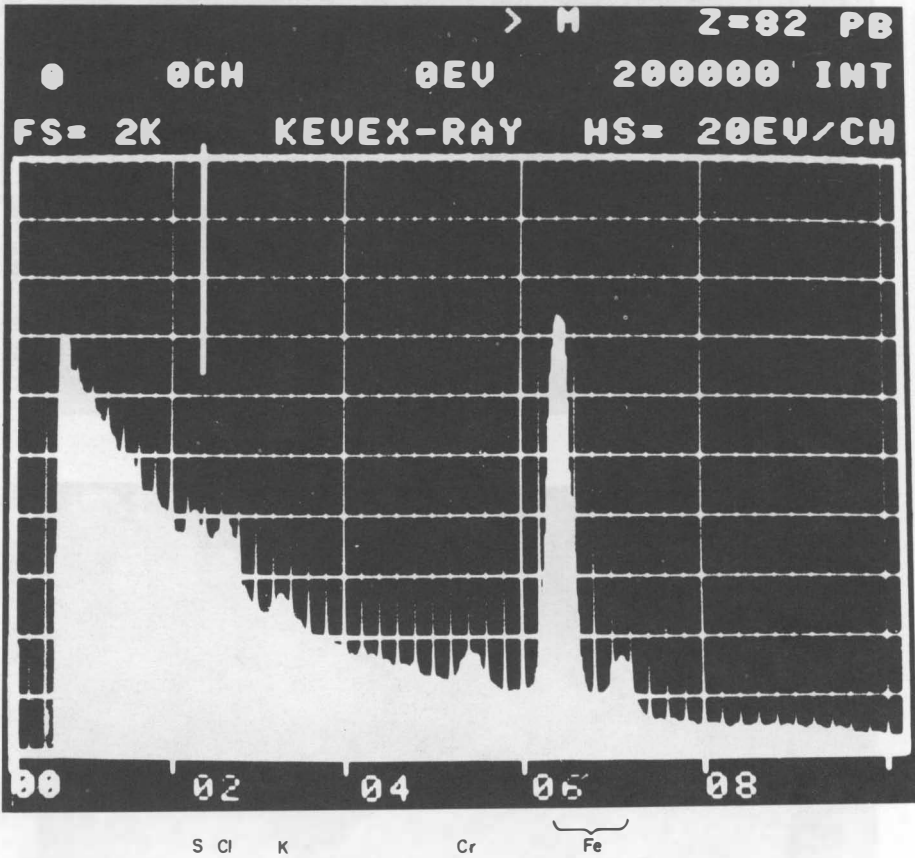


FIGURE 26 WAVELENGTH DISPERSIVE X-RAY ANALYSIS CHART  
 OF HARD B SCALE FROM INSIDE SURFACE AREA.

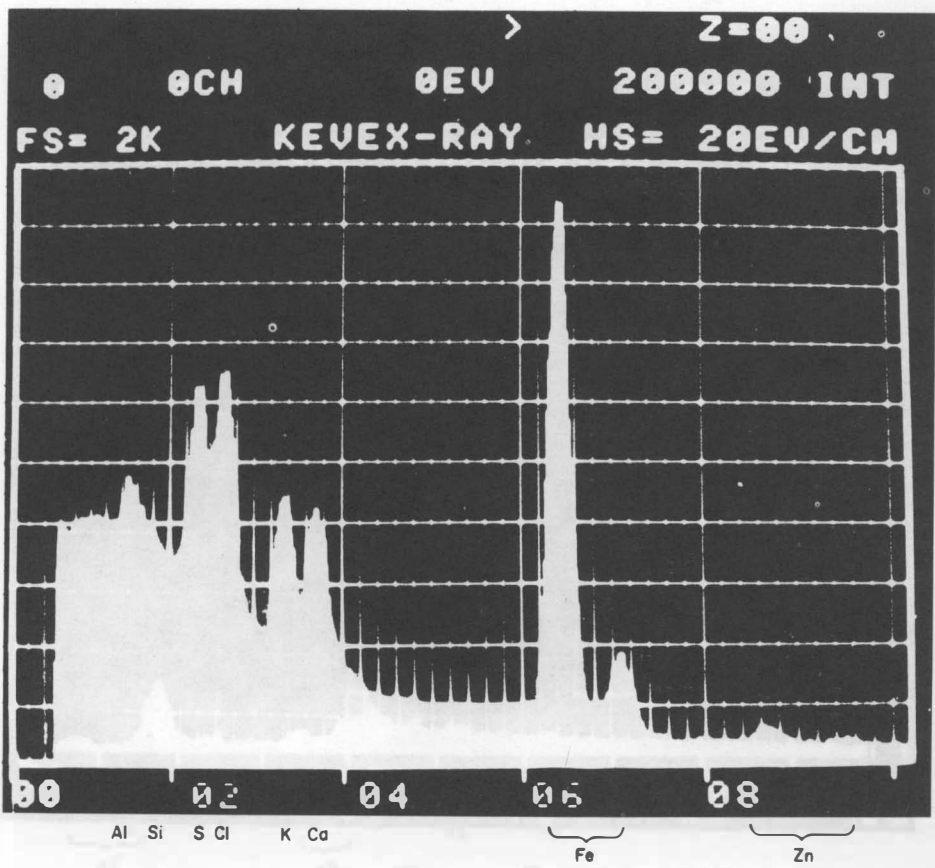


FIGURE 27 WAVELENGTH DISPERSIVE X-RAY ANALYSIS CHART  
 OF HARD B SCALE FROM CROSS-SECTION AREA.

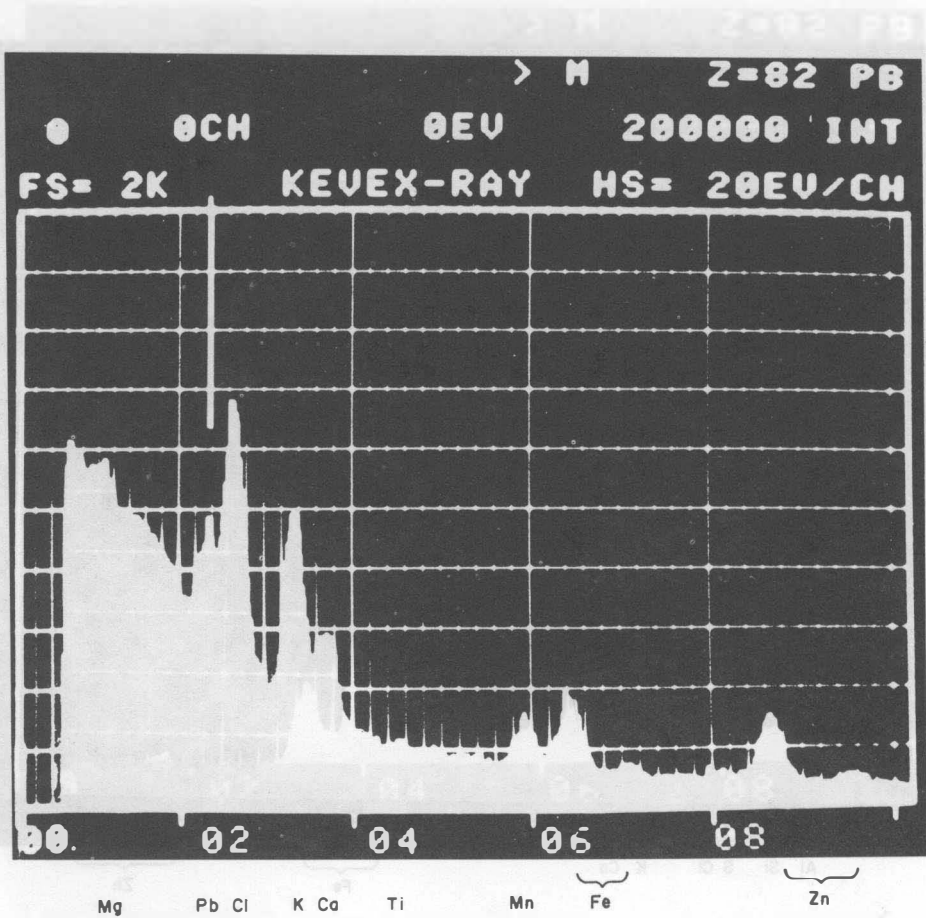
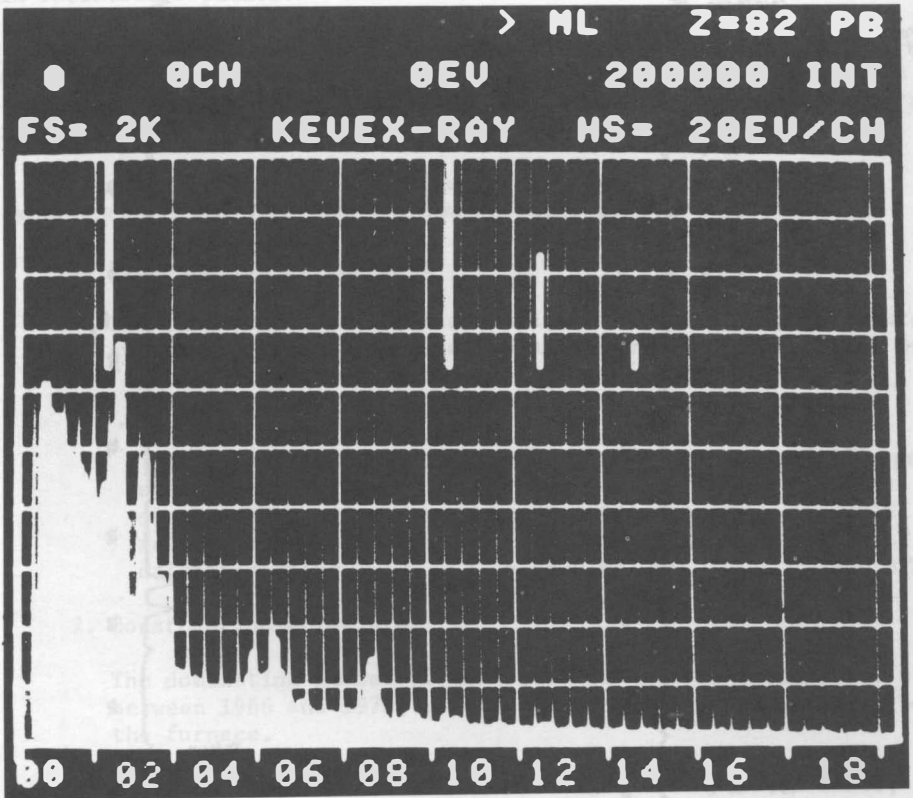


FIGURE 28 WAVELENGTH DISPERSIVE X-RAY ANALYSIS CHART OF HARD B SCALE FROM OUTSIDE SURFACE AREA.



Pb Pb Pb

FIGURE 29 WAVELENGTH DISPERSIVE X-RAY ANALYSIS CHART OF HARD B SCALE FROM OUTSIDE SURFACE AREA.



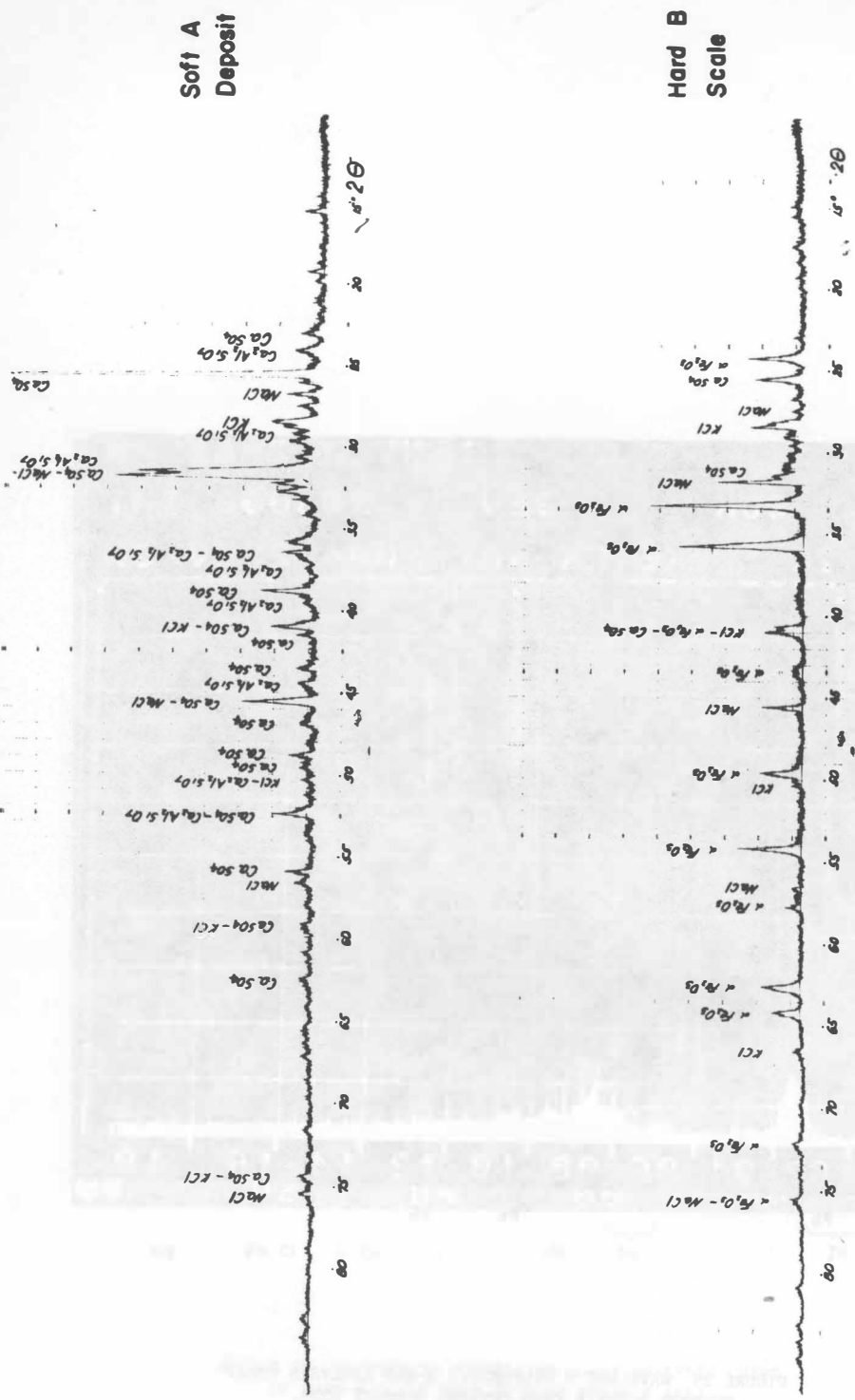


FIGURE 30 X-RAY DIFFRACTION CHART OF SAMPLES.